INVESTIGATING STRAINED $SrTiO_3$ FILMS ON SI USING X-RAY DIFFRACTION

by

John T. Miracle, B.S.

A thesis submitted to the Graduate Council of
Texas State University in partial fulfillment
of the requirements for the degree of
Master of Science
with a Major in Physics
August 2019

Committee Members:

Nikoleta Theodoropoulou, Chair

Alexander Zakhidov

Casey Smith

FAIR USE AND AUTHOR'S PERMISSION STATEMENT

Fair Use

Duplication Permission

ACKNOWLEDGEMENTS

The work in this thesis was made possible by NSF Career Award DMR-1255629.

I would like to thank the faculty and staff of Texas State University Department of Physics for providing a welcoming learning environment. Special thanks go to the SRO staff for providing a robust and well managed research environment that allowed me to readily acquire the knowledge and skills to complete the work in this thesis. They also deserve thanks for providing me with quality employment that both provided the ability to continue pursuing my education and the opportunity to teach and gain many hands-on hours with a variety of equipment.

I am especially grateful to the following people:

My parents John and Linda for encouraging me to pursue my talents in the life of a scientist.

My daughter Kiary for understanding the importance of the late nights away from home and being always ready with a smile and a hug.

Dr. Wim Geerts for encouraging me to return to Texas State and continue my graduate studies.

Dr. Ryan Cottier for developing the expertise on MBE technology and growing the samples used for this thesis.

Dr. Alex Zakhidov for introducing me to an open laboratory environment to pursue experimental science with a team.

Pete Walker for teaching me the basics of X-ray diffraction.

Dr. Casey Smith for being truly present and hands on with help in every area of research I've tried since starting my master's degree. His help allowed for the smooth advancement in skill that would have been haphazard and stilted otherwise, especially with advanced techniques in XRD metrology.

Dean Koehne for teaching me the ins and outs of device processing and instrumentation, and for always being there to help me out of tight spots I got myself into.

Dr. Nikoleta Theodoropoulou for teaching me to science! Without her guidance and support this thesis would not have happened; it was through her encouragement that I became an experimentalist and decided to continue my master's on a thesis track.

TABLE OF CONTENTS

Page

LIST OF TABLES

Table **Page**

LIST OF FIGURES

Figure **Page**

LIST OF ABBREVIATIONS

Abbreviation	Description
RHEED	reflection high-energy electron diffraction
PZT	lead zirconate titanate
MBE	Molecular Beam Epitaxy
ML	monolayer
FE	ferroelectric
EXAFS	extended X-ray absorption fine-structure
nm	nanometers
PO_2	Oxygen partial pressure
XRD	X-ray diffraction
TMO	transition metal oxide
VRH	Variable Range Hopping
EEI	electron-electron interaction
ES	Efros Schklovskii
QW	Quantum well
STO	$SrTiO_3$
XRR	X-ray reflectivity
FWHM	full width half max
SOI	Spin-Orbit interaction

I. INTRODUCTION & MOTIVATION

Introduction

Oxide heterostructures based on $SrTiO_3$ have been a discovery ground for emergent physical phenomena, most notably conductivity at the interfaces between insulators [1, 2]. The 2-dimensional electron systems at the surface of $SrTiO_3$ [3], at the interface between $SrTiO_3$ and oxides [1], and in δ-doped $SrTiO_3$ [4] have been investigated intensely in the past decade. At the $SrTiO_3$/$LaAlO_3$ interface, quantum confinement effects and a tunable spin-orbit interaction (SOI) have been demonstrated[5-7].

$SrTiO_3$ is for oxides what Si is for semiconductors, not only because they are the most well-studied systems in oxides and semiconductors respectively but because of the tunability of the electronic properties and functionalities that constitute them ideal for technological applications.

In 1998, McKee and co-workers achieved the direct epitaxial growth of single crystal perovskite $SrTiO_3$ on Si(001) using a submonolayer of Sr as a template deposited at 600 °C on a clean 2x1 Si(001) reconstruction using reflection high-energy electron diffraction (RHEED) [8]. $SrTiO_3$ remains the only oxide material that can be directly grown on Si(001) epitaxially. The epitaxial growth of $SrTiO_3$ on Si(001) has been thoroughly studied since 2000 in hopes of integrating a high k dielectric with Si technology. $SrTiO_3$ on Si can also serve as a virtual substrate for the growth of various other functional oxides such as $BiFeO_3$ [9] or PZT (lead zirconate titanate) [10] so complex oxides grown directly on Si by Molecular Beam Epitaxy (MBE) can also be exploited for additional functionalities such as ferroelectricity, ferromagnetism,

piezoelectricity, and pyroelectricity. This is critical because these functionalities can enable far-reaching applications in advanced memories, sensors, and persistent surveillance and radar technologies. Furthermore, recent advances after the discovery of new physical phenomena in epitaxial oxide heterostructures and their interfaces [1] have led to an enhanced understanding of these novel functionalities, opening up broader opportunities for fundamental understanding by the scholarly community and societal technological impact.

Understanding the complex materials chemistry that takes place during this heterosynthesis, controlling the oxide layer nucleation and regulating the growth remains a challenging task. Most of the investigations focus on the effect of the growth conditions on the structural characteristics; electronic transport has been scarcely explored.

Our group has been investigating the growth, structural, electronic and optical properties of strained $SrTiO_{3-\delta}$ thin films grown epitaxially on Si (001) wafers. This is a largely unexplored system in terms of its optoelectronic properties and given the attention focused on the interface between $LaAlO_3$ and $SrTiO_3$, it merits investigation not only because of the technological relevance of its material constituents, Si and $SrTiO_3$, but also to understand the fundamental physics.

We have been investigating the electronic properties of correlated oxides using low-temperature magneto-transport measurements. We have demonstrated that the temperature and magnetic field dependence of the conductivity is dominated by two-dimensional quantum effects. We have observed physical behavior that has also been reported for the $LaAlO_3$ and $SrTiO_3$ system such as Spin-Orbit Coupling that may have

far-reaching implications for the field of spintronics. Additionally, we have seen effects that have not been observed in bulk $SrTiO_3$ or other $SrTiO_3$ based systems such as correlated behavior. Electronic quantum coherence below 100K is observed for all growth parameters. Quantum confinement, strong electron correlations, Zeeman spin-splitting, and spin-orbit coupling are all manifested in the electronic transport of the $SrTiO_3$/Si system for different carrier concentrations, growth conditions, film thickness and strain. We have been tracing a very rich phase diagram for this quite simple but not simplistic system of epitaxial $SrTiO_3$ film grown directly on Si(001).

$SrTiO_3$ on Si

The extreme sensitivity of oxide properties to structural distortion can be used to tailor these physical and electronic properties by exploiting the epitaxial strain of thin films and heterostructures. Strain can enhance the transition temperatures in ferroelectrics [11] [12], enhance magnetism and superconductivity [13] and increase correlations [14].

$SrTiO_3$ forms in a cubic lattice at room temperature with a lattice constant of $a = 3.905$ Å. Coherent growth on Si(001) ($a = 5.431$ Å) can be achieved using MBE by a 45° rotation around the surface normal, $SrTiO_3$[001] || Si[001] & $SrTiO_3$[100] || Si[110] [15]. This results in 1.7% compressive in-plane strain at 300 K [16, 17]. The structure is shown in Figure 1.

X-ray fine structure measurements of 5 monolayers (ML) of $SrTiO_3$ on Si reveal that the strain induces a tetragonal distortion of the oxygen octahedral cage with ferroelectric (FE) distortion displacement of the Ti atoms along the z-axis. The FE

distortion causes splitting of the t_{2g} levels with the d_{xy} band edge lower in energy than the elliptical d_{zx} and d_{yz} bands and induces a large polarization [18]. In addition, $SrTiO_3$ goes through an antiferrodistortive phase transition at 105 K and the orthorhombic distortion due to the rotations of the oxygen octahedra further increases the splitting of the t_{2g} states.

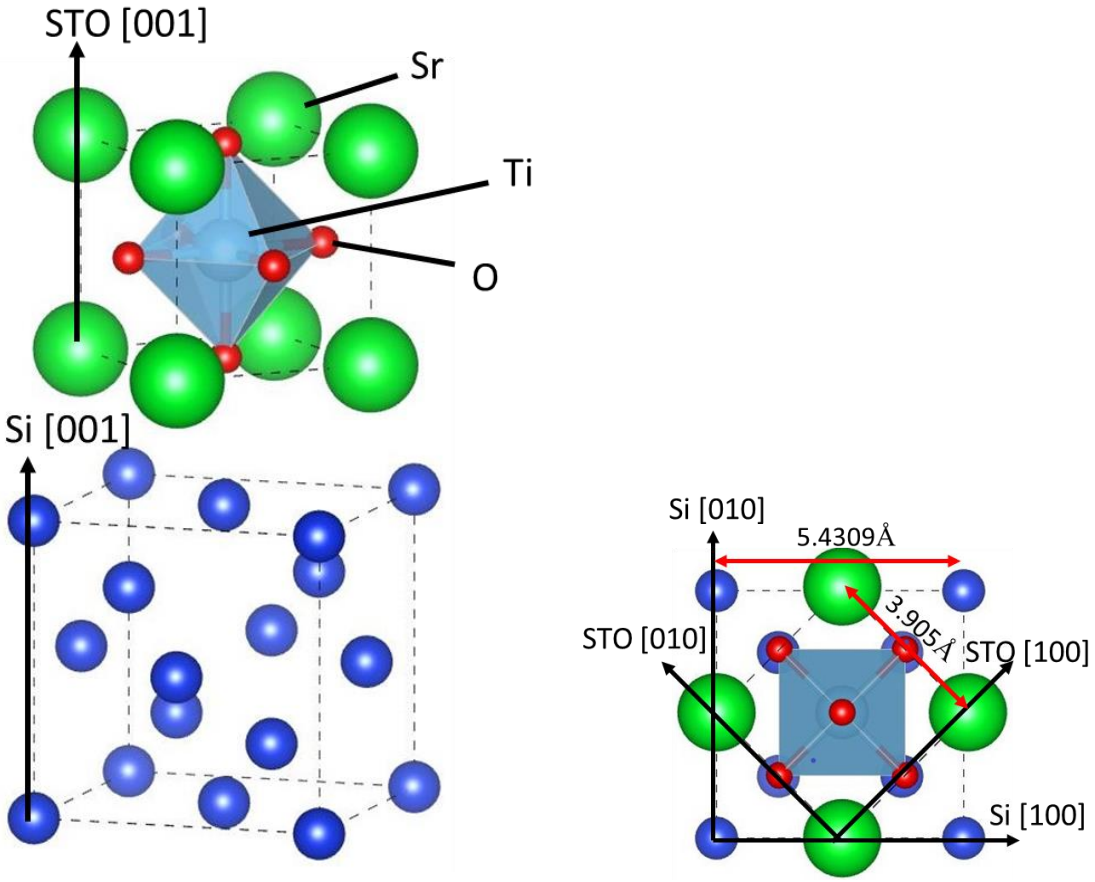

Figure 1: Crystal structure of $SrTiO_3$/Si.

Extended x-ray absorption fine-structure (EXAFS) data indicate a polarization of $SrTiO_3$ for 4-6 nm $SrTiO_3$/Si that decreases away from the interface. The observed polarization is attributed to a modulation of the out-of-plane Ti-O bond length by 0.22Å

[16]. Strain causes FE at room temperature when the $SrTiO_3$ thickness is less than 4nm[12]. Below the critical thickness, $SrTiO_3$ grows on Si coherently [12]. As thickness increases, the lattice relaxes to the bulk $SrTiO_3$ crystal structure through misfit dislocations. The relaxation mechanism is sensitive to the exact growth procedure with a loss of coherency above ~9 nm for high O_2 partial pressure (PO_2) and ~14 nm for low PO_2 [12] [17].

In general, understanding the process of strain relaxation of $SrTiO_3$ on silicon will be useful for controlling the $SrTiO_3$ lattice constant for lattice matching with functional oxide overlayers. In our case, we have strong evidence that the $SrTiO_3$/Si system is driven to an insulating state through electron-electron correlations and $SrTiO_3$ becomes a Mott insulator for films less than 14 nm thick. This is the first observation of turning $SrTiO_3$ from a band insulator to a Mott insulator. Low electron concentrations (~$5x10^{12}$ cm^{-2}), epitaxial strain (evaluated using x-ray diffraction (XRD)) and quantum confinement seem to play an important role in strengthening electronic correlations.

The goals of the detailed XRD measurements and analysis presented here are specific to our group's research objectives and are tailored for the study of ultra-thin epitaxial $SrTiO_3$ (001) films on Si(001):

1. Evaluate the crystalline quality the epitaxial $SrTiO_3$ films
2. Understand the effect of the *nontrivial* oxide-MBE growth conditions on the crystalline properties of the films
3. Correlate the observed electronic behavior to crystal structure and more importantly to the strain and strain relaxation mechanisms.

Growth

$SrTiO_3$ films were grown on semi-insulating p-Si(001) substrates via oxide MBE using Ti and Sr effusion cells for co-deposition with a base pressure of $\sim 10^{-10}$ Torr and an O_2 partial pressure of $4 \times 10^{-8} - 4 \times 10^{-7}$ Torr resulting in slightly Oxygen deficient films with carrier concentrations determined by the combination of PO_2 and growth rate. The exact growth procedure including the Si de-oxidation process is described in [19]. The surface quality and stoichiometry were monitored continuously using *in-situ* RHEED. The samples are Ti-terminated and were not annealed post-deposition to avoid the formation of SiO_2 at the interface. The films were atomically flat measuring the surface roughness using Atomic Force Microscopy.

The first set of films consists of the four films: S1-S4. S1, S3, and S4 are grown under different Oxygen conditions and have similar thickness. The second set of films consists of three films: S5-S7. The films are all thicker than those in the first set and were grown under very similar conditions with the Oxygen pressure slightly higher for S7. We present growth parameters for the seven films in Table 1.

Table 1. Growth Parameters

Sample	Timestamp	p-Si(001) resistivity (Ohm-cm)	Th (XRR) (nm)	Rate (nm/min)	PO2 (Torr)	Tsub (˚C)
S1	130722-03	1-10	8.6	0.35	4.0E-07	500
S2	130626-01	1-5	13.2	0.45	4.0E-07	500
S3	130717-04	1-5	9.4	0.42	2.0E-07	500
S4	130717-03	1-5	9.2	0.37	8.0E-08	500
S5	161206-01	1-5	23.3	0.28	4.6E-08	500
S6	161207-01	0.1-0.5	21.3	0.25	4.5E-08	500
S7	161208-01	5-10	20.8	0.24	5.3E-08	500

Transport Properties

We are outlining some of the results of the films without going in depth in terms of the analysis and 2d physics that we observe. The goal is to illustrate the electronic behavior and how it can be correlated to the structure and XRD studies.

1st Sample Set (Thin Samples)

Undoped $SrTiO_3$ has d^0 electron configuration and is therefore termed as a "band insulator" but correlation effects become important when it is doped with electrons[20]. Typical Mott insulators include many of those transition metal (4d-, 4f-, 5f-) oxides (TMOs). According to band theory, most of these TMOs would be metals with partially filled d or f bands. However, many are insulators due to electron correlations. In a Mott insulator, the ratio between the typical strength of Coulomb repulsion (U) and the typical kinetic (Fermi) energy of the itinerant electrons or bandwidth (W), U/W is large. The Mott metal-insulator transition can be induced by tuning the relative magnitude of the Coulomb repulsion U to the bandwidth W at fixed band-filling (half-filling), which is called bandwidth-controlled metal-insulator transition. One example of this is applying stress on a Mott insulator to change the atom spacing and consequently bandwidth to induce a metal insulator transition without changing the carrier density [21].

We have strong evidence that the $SrTiO_3$/Si system is driven to an insulating state through electron-electron correlations and SrTiO3 can become a Mott insulator for films with thickness less than 14nm. This is the first observation of turning $SrTiO_3$ from a band insulator to a Mott insulator. Low electron concentrations (~$5x10^{12}$ cm^{-2}), epitaxial

strain (evaluated using XRD) and quantum confinement seem to play an important role in strengthening electron correlations.

The sheet resistance, R_s of all samples increases as the temperature is lowered (Figure 2a). We focus on temperatures below 40 K to avoid phonon and substrate contributions. The conductivity (σ=1/ R_s) is logarithmic in temperature (Figure 2b), characteristic of 2d quantum corrections to the conductivity and provide evidence of a 2d electron system with quantum phase coherence. Below 10 K, R_S increases abruptly and can be described by Mott-Variable Range Hopping (VRH) [22]. The data are well linearized in the coordinates lnR_s and $T^{-1/2}$ with two fitting parameters: T_{ES} (values shown on Figure 2c) and $R_{ES} \sim \frac{h}{2e^2} \equiv R_K/2$ (roughly sample-independent). T_{ES} reflects the effective strength of Coulomb interactions such that the stronger the electron-electron interaction (EEI), the higher the crossover temperature to Efros Shklovskii -VRH (ES-VRH) [23] and correlates with K_{ee}. Even more, when $ln(R_S/R_K)$ is plotted against the dimensionless parameter $(T_{ES}/T)^{1/2}$, all traces of Figure 1c collapse onto a single line with an intercept of 1/2. Thus, the insulating behavior is best described by ES-VRH, a manifestation of the Coulomb gap (depletion of states) induced in the single-particle density of states at the Fermi level by Coulomb interactions

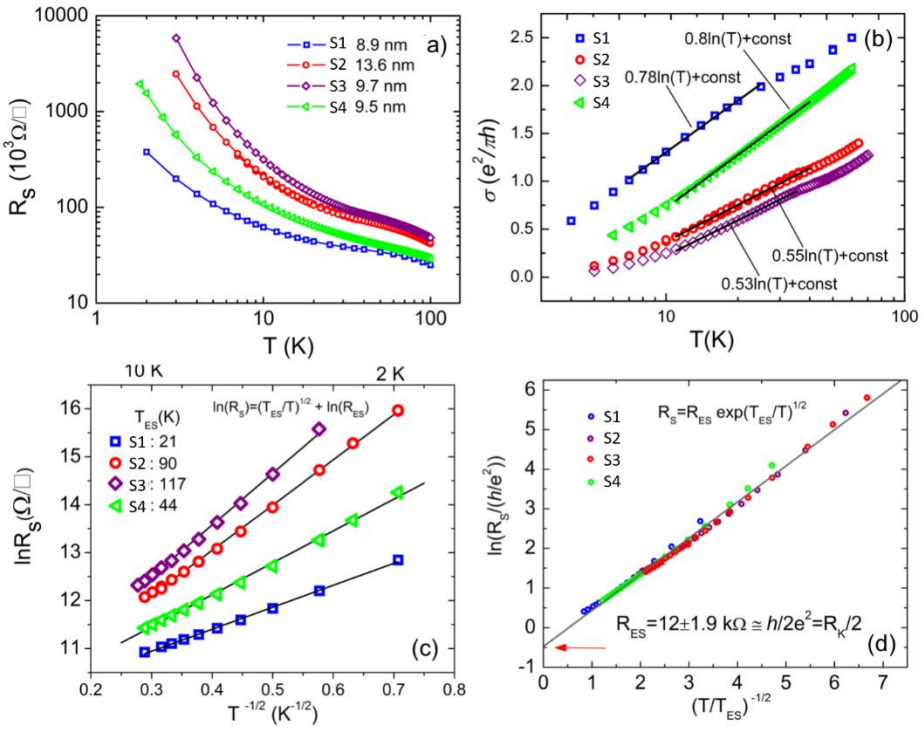

Figure 2: Electronic transport behavior for S1-S4 demonstrating 2d transport and Mott insulator behavior.

A Mott insulating phase is predicted for $SrTiO_3$ for large distortions of the crystal structure with Ti-O-Ti angles of 165° compared to 180° in the cubic phase and for a high doping level of 0.5 electron per Ti atom [24]. Additionally, models that include full-range Coulomb forces predict that t_{2g} electrons at low concentrations in $SrTiO_3$-based interfaces or quantum wells (QW) follow spontaneous orbital and spin order exhibiting correlated behavior[25, 26]. Thus, understanding the effect of structural distortion and strain for this set of films is crucial.

2nd Sample Set (Thick Samples)

The resistance of the second set of samples shows a logarithmic temperature dependence below 20 K. The slope from the logarithmic in T fit is a measure of the

strength of Coulomb interactions in this system. This set of samples is not becoming insulating at low temperatures and the effect of electron-electron interactions is more subtle. One of the most important features is the 2d behavior as evidenced by the lnT dependence of the conductivity (Figure 3) and the magnetoresistance (not presented here). The estimated effective thickness of the electrons at low temperature is 2-4nm and of the same order as the coherently strained layer.

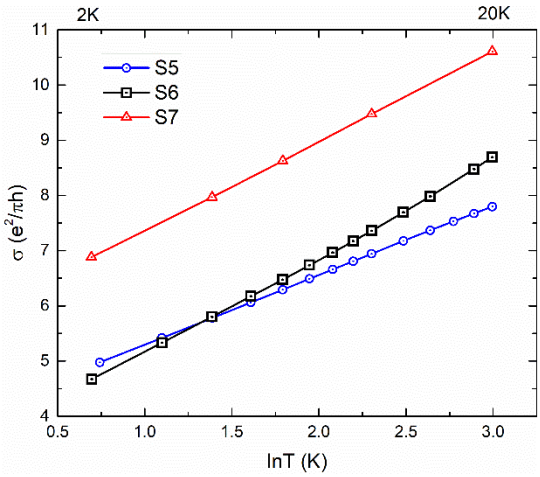

Figure 3: Conductivity vs. temperature for S5-S7 demonstrating 2d transport behavior.

II. MEASUREMENT TECHNIQUES

X-Ray Diffraction

X-ray diffraction is a technique in which monochromatic x-rays with wavelengths on the order of interatomic distances (~1Å) are made to interfere by scattering off the electrons associated with the atoms in a material. Usually this is a solid, but the technique can be extended to liquids and gases. The most studied and highly refined application is in the analysis of crystalline solids and particularly in materials research. For this thesis it will be employed to determine the structural properties of thin films of $SrTiO_3$(STO) grown on Si.

Figure 4 is a simple model used to describe the interference effects of diffraction from within a perfect crystal lattice. The scattering geometry is treated as the symmetric reflection from multiple parallel planes with constant interplanar distance. As is typical of diffraction geometries the x-ray source and detector are sufficiently far enough away, and the distance being probed sufficiently small, that the beam is treated as being perfectly parallel. In the case that the path length difference between the x-rays scattered from subsequent planes is equal to an integer number of wavelengths of the x-rays, there will be constructive interference. Thus, a relationship can be determined which relates the spacing in the crystal parallel to the scattering vector and surface normal to the characteristic wavelength of the x-rays. This relationship is described by the Bragg equation and is used to analyze measurements with a monochromatic x-ray source and a precise goniometer to investigate interatomic spacing in crystals.

$$n\lambda = 2dSin(\theta) \quad \text{The Bragg equation}$$

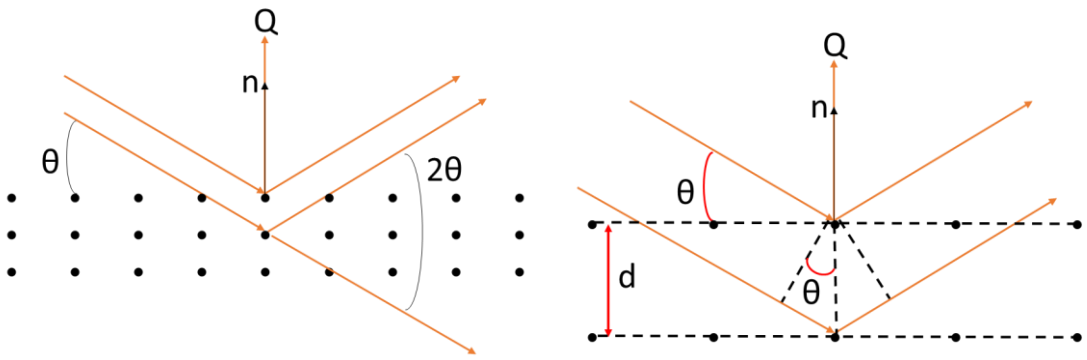

Figure 4: Atomic scattering diagram of XRD demonstrating the parameters of the Bragg equation.

Specular Scattering and Mirror Surfaces

In general, any set of atoms that can be defined by a set of parallel planes can be investigated with diffraction. These lattice planes can be treated as mirror planes subject to specular scattering. When the scattering satisfies the Bragg equation, the diffracted intensity reveals information on the characteristics of the set of crystal planes being investigated. This includes the interplanar spacing, the relative distribution of this spacing, and along with precise knowledge of the geometry from the goniometer, the orientation with respect to the surface normal and the presence of defects.

Symmetric Measurements

So far symmetric reflection geometry has been discussed. Experiments utilizing this geometry investigate the interatomic properties of the crystal parallel to the surface normal. Considering the twin cubic crystal systems of STO on Si under investigation here it is convenient to define the orientation of the lattices with respect to their out of plane lattice parameters. Herein after the lattice parameters and orientations of the STO film and Si substrate will be referred to as defined in the introduction.

The system is grown such that the out-of-plane axes (c-axes) of each crystal are colinear (STO[001]//Si[001]) and form the principle orientation of the system. The in-plane axes of STO are rotated by 45° with respect to those of Si (STO[100]//Si[110]) in order to accommodate the in-plane lattice spacing mismatch. Thus symmetric measurements probe the STO(00L) and Si(00L) families of planes.

XRR

A technique called X-ray reflectivity (XRR) is employed to investigate whole film morphology which does not rely on interatomic scattering, but instead on the scattering of x-rays from the surface and the STO/Si interface of the system. This method follows similar development as the Bragg equation, except that instead of determining the interatomic spacing it determines the interplanar spacing of stacked films (Figure 5). This measurement relies on angles very near the critical angle and is heavily influenced by specular reflection and refraction at the surface.

This is the straightest forward technique optically. It requires a flat sample and substrate, but little else. It is insensitive to orientation and lattice morphology and is primarily used to determine properties including thickness, roughness, and density.

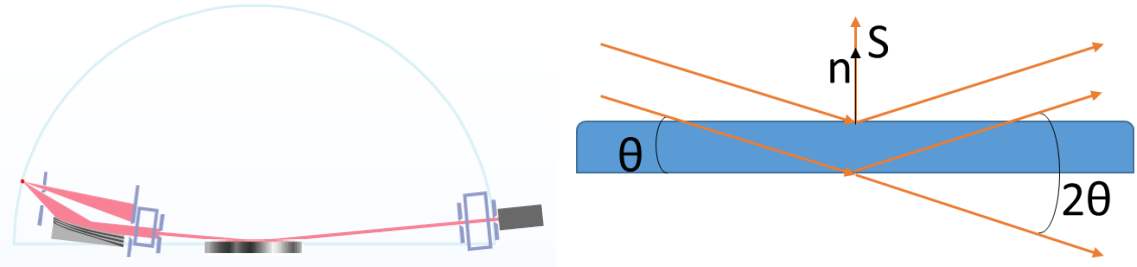

Figure 5: XRR optical setup.

Normal Surveys

This is the principle investigatory technique with regards to the crystal properties of a system. For thin films it is used to interrogate the out-of-plane lattice parameters, crystal orientation, and possible defect properties in the film. For our system we have only one family of planes for each crystal oriented with the surface. The scattering probabilities, which are described by the structure factors of the system, are determined in relation to the specific arrangements of atoms within the unit cell of the crystal and reference specific scattering trajectories. Certain structure factors are zero and do not contribute to diffraction when the scattering geometry satisfies those conditions. This is not significant for STO, but the only allowed out-of-plane lattice plane that should show up for Si is the (004) reflection. This is not entirely true, as the "forbidden" Si(002) and (006) peaks appear to show up for [001] oriented Si substrates. This anomaly comes from what has been described as multiple internal reflections which accumulate to act like these peaks[27]. They are however easy to recognize and do not impact the measurement in any way.

The measurement proceeds as diagramed in Figure 6. The angle between the incident beam and the detector is called 2θ because the detector is moved at a constant rate twice that of the incident angle of the source beam with the sample surface From this technique the phase of STO(00L) can be confirmed and the out-of-plane lattice parameter can be determined using the Bragg equation.

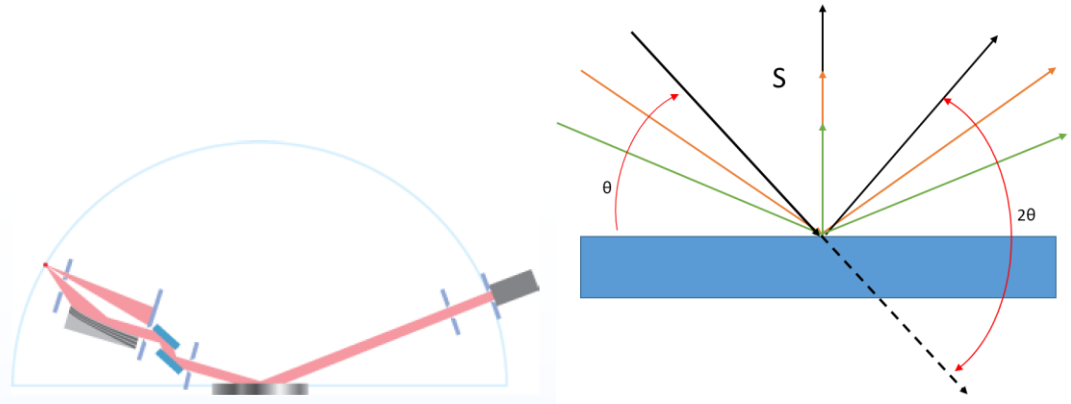

Figure 6: XRD optical setup.

Coupled Scans

Focusing in on one Bragg peak, aligning carefully to the peak position using multiple orthogonal axes of the goniometer, and taking a slow and precise scan is called a coupled 2θ/ω scan. The conditions are very near, if not exactly oriented with the sample surface, but alignment unlocks the coupling between the incident beam inclination to the sample surface and that of the detector; thus, the name 2θ/ω instead of precise θ/2θ. These scans are called couple scans because the incident and diffracted beam directions are still coupled such that the scattering direction is held constant: so, a specific peak can be investigated without having to necessarily be obligated to the surface normal. These scans are the basis for the asymmetric scans introduced later.

This measurement is used principally to provide a precise measurement of the lattice parameter associated with the peak and determine if there is any distribution of the out-of-plane lattice spacing. Further information can be garnered as to certain material properties from shift in the peak position from that of a referenced bulk material, broadening of the peak profile, and possible interference fringes around these peaks called Laue or Pendellosung fringes.

Peak shift is an immediate indication of strain or relaxation in an epitaxial film and can be applied with respect to a known reference to determine the lattice parameters of a film containing no other defects. The broadening of a peak profile is a convoluted process that arises from many different sources. Very thin films exhibit peak broadening due to a combination of strain and a short order effect which simply put eliminates a portion of the destructive interference associated with deviation from the Bragg condition for large perfect crystals. This will be discussed more later.

The most striking features of these peaks are the interference fringes on either side. These so called Pendellosung fringes (because they exhibit behavior like that of a compound pendulum) are the result of half wavelength interference very similar to single slit diffraction. This interference arises from partially out of phase scattered waves which accumulate to destructive interference over several lattice planes with termination determined by a very sharp interface with the substrate. For this simplified case in which we only have one principle lattice axis contributing to the peak, their functionality is described by the Laue equation:

$$I^2 = F^2 \frac{Sin(2\pi cN \frac{Sin(\theta - \theta_B)}{\lambda})}{Sin(2\pi c \frac{Sin(\theta - \theta_B)}{\lambda})},$$

Where I is the scattering amplitude, F is the structure factor associated with that specific Bragg condition, c is the associated lattice parameter, N is the number of planes, θ_B is the associated Bragg angle, and $\theta = 2\theta/2$ is the independent scan variable. This equation applies to thin films on the order of the thickness of the films presented in this thesis and can be used to accurately determine the film thickness like the XRR measurement. A technique is employed herein called extended rocking curve analysis in which these

fringes along with peak shift are fit with reference to the principle substrate peak in order to accurately determine the lattice constant(s), percent relaxation, and film thickness at the same time. Of note is that these fringes only arise with a consistent lattice parameter (not constant, but close) and a very sharp flat interface, so their existence alone evidences these attributes[28].

Rocking Curves

Following the same alignment performed for the coupled scan, this technique investigates the variation in the lattice parameter with regards to uniformity and orientation. Mosaicity and dislocation defects are the principle contributors to peak broadening in relaxed films. Once the system is focused on a Bragg peak, the scattering vector associated with the measured crystal spacing is held constant by holding 2θ constant and either tilting the sample or moving the "2θ -locked" source and detector arms together to simulate tilting (Figure 7). This is called an ω rocking curve, because the sample is rocking underneath the detector held to measure at a specific Bragg condition.

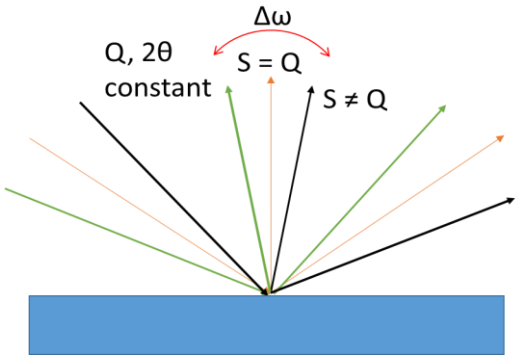

Figure 7: Rocking curve optical setup.

This technique can determine how laminar the planes in the crystal are, whether there is any tilt, and generally gives an indication of crystal quality. Sharp peaks in this scan indicate that the lattice is very uniform, while broad peaks are evidence of possible mosaicity, misorientation, sample curvature, or a large strain or stoichiometry gradient causing a gradient in the lattice spacing out of the plane. Since they rely on the same alignment and complement each other, these last two techniques are usually performed together.

Asymmetric Measurements

Due to the 45° rotation between STO and Si there is only degeneracy in the out-of-plane and in-plane orientations between the two crystals; there is no degeneracy for any asymmetric orientation. This effectively limits the use of some very useful advanced diffraction techniques that rely on these geometries in order to differentiate the effects on the film in and out of the plane with respect to the substrate. Since direct in-plane measurements are impractical, if not entirely impossible, for typical laboratory diffractometers like the one used here, a confluence of measurements is necessary to extrapolate the details we need to clarify the questions that brought us here.

Asymmetric scans start similarly to the coupled scans in that alignment is performed in order to observe Bragg diffraction from a set of parallel planes. The exception is that there is now an angular dependency to the penetration depth and two more degrees of freedom in searching for the peaks. The penetration depth becomes ever shallower as the inclination is moved away from the surface normal. This is useful for determining a changing lattice parameter with respect to depth, eliminating contributions

from the out-of-plane parameter, and fully characterizing relaxation contribution from in and out-of-plane strains. The difficulty here lies in the thinness of the films studied and the intensity limitations of a lab-based diffractometer. For such thin films, and at such low angles to the surface, the signal falls below the noise and no discernable peaks are attainable.

So, it is necessary to keep the inclination relatively high, but another benefit of this geometry is degeneracy within the individual crystals. For these cubic systems there is 4-fold, 90° rotational symmetry for the principle in-plane axes and symmetric combinations of the two. This allows for determination of epitaxial growth and single crystallinity in these samples along with the ability to calculate in-plane lattice constants with respect to the out of plane constant already directly measured.

Rocking Curves

All asymmetric scans hinge on knowing the orientation of your sample or taking the time to find it. Finding it involves hunting for a peak with the expected Bragg condition and inclination held constant and the sample being rotated about the surface normal until the peak is found. This is essentially what the subsequent rotational survey does, but for now it's just to find a peak. Once that peak is found, refinement in the same way as that used for a coupled scan is performed to align to the Bragg condition, then a coupled scan at this asymmetric position is taken. A diagram of the Bragg condition for an asymmetric peak is shown in figure 8.

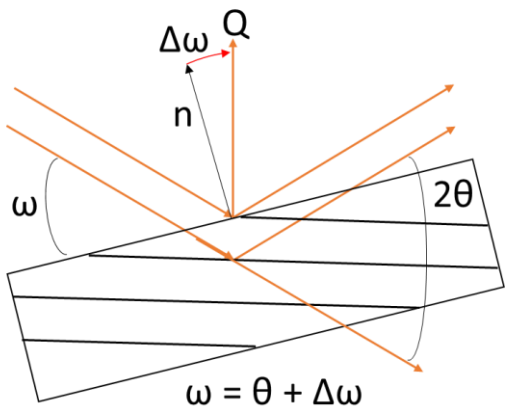

Figure 8: Asymmetric scan diagram.

Rotational Surveys

Subsequent to finding and aligning to an asymmetric peak, the sample is measured by rotating about the surface normal to find all the degenerate peaks (Figure 9). This is repeated for both the film and the substrate during the same sample mounting to find the relative orientation between them and determine heteroepitaxy and single crystallinity.

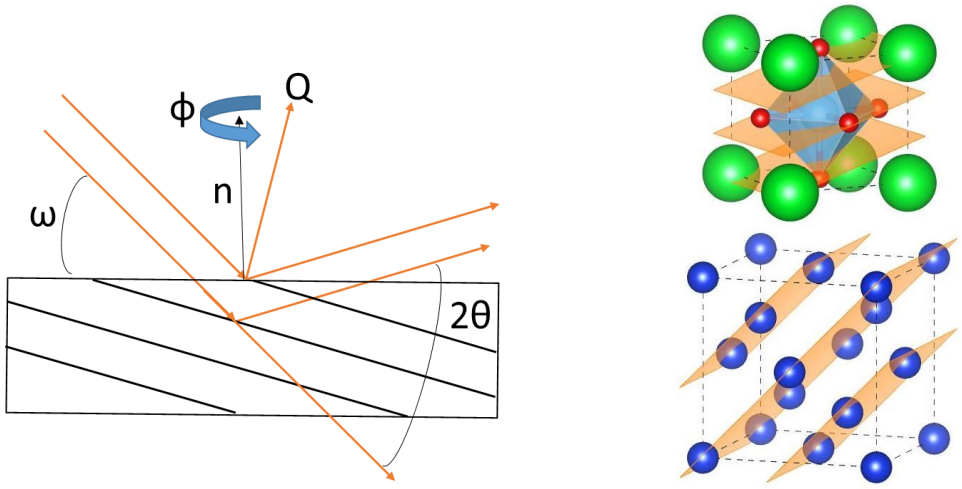

Figure 9: Rotational φ survey diagram and lattice plane example. The crystal structure on the right shows the Si(202) planes on bottom and STO(103) planes on top.

III. ANALYSIS

Equipment and Settings

All measurements were taken using a 4-circle Rigaku SmartLab Diffractometer equipped with a HyPix-3000 Hybrid Pixel Array Detector. The 4-circle geometry is capable of aligning to the scattering geometry for any plane oriented in the hemisphere above the sample stage. The instrument schematic is shown in Figure 10. The HyPix detector is capable of being operated in 0D, 1D, and 2D collection modes. The 1D and 2D modes separate the detector into regions in which the pixels are treated as a variable array of individual detectors. The 0D mode is the most common collection mode in which the entire array is integrated and treated as the intensity at the center of the detector. All measurements taken for this thesis were collected using 0D mode with high resolution optics provided by a Ge (220) two-bounce monochromator.

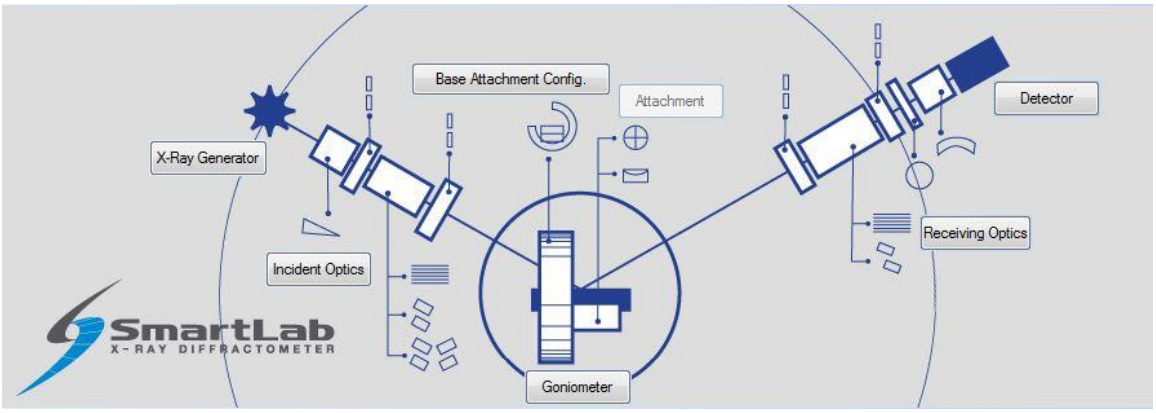

Figure 10: Rigaku SmartLab diffractometer schematic.

The XRR measurements were taken with very narrow (0.05mm) optical slits in the diffraction plane and very narrow receiving slits in general. These slits define the beam width and influence the divergence of the beam and possible resolution of the

measurement. The very small incident angles used in reflectivity measurements result in scattering dominated by specular reflection; most importantly, however, the sensitivity of this technique to small variations in scattering angle due to film thickness being probed in the same orientation as the beam divergence. This necessitates the use of as narrow a beam width as possible in order to minimize this complication.

All other measurements were taken with 1mm vertical slits. The incident angles for diffraction measurements are all large enough that the resolution is dominated by the sample and not the beam divergence. For example, referring to the resolution curve for the Ge-(220)x2 monochromator from Figure 11, two spots are marked on the curve at the angles where XRR measurements are collected (0-5°) and for the principle diffraction peak from the $\omega/2\theta$ coupled scan (STO(002) near 23°). The instrument resolution near 23° is ~0.004° which is orders of magnitude narrower that any full width half max (FWHM) collected for this thesis. Peak widths at that resolution are typically associated with powder samples with near perfect crystallinity. This allows for the use of wider slits and commensurate integration areas on the sample and detector that strike a balance between maximizing resolution and loss of intensity. The table below contains the slit settings for each setup.

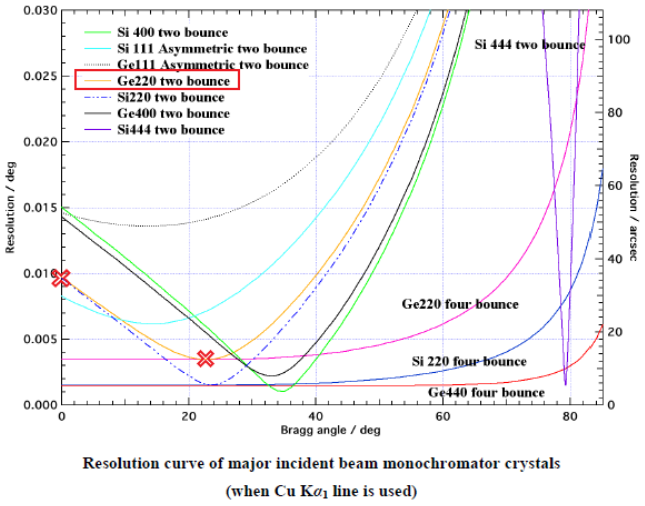

Table 2. Diffractometer Settings		
Optical Parameters	XRR	XRD
Resolution optics	Ge-(220)x2	
Slit widths in mm		
Incident slit width	0.05	1.00
Incident slit height	2.00	1.00
Receiving slit width	0.15	1.00
Receiving slit height	0.10	1.00

Figure 11. Resolution curve for Ge(220)x2 monochromator..

Single peak data analysis was performed using Origin Pro 2019 (θ/2θ survey, ω rocking curve) and the software package GlobalFit which came as part of the Rigaku data analysis suite was used for the oscillatory fittings. The Gaussian and Lorentzian fitting of individual peaks is handled readily by origin. GlobalFit is specifically designed to analyze the oscillatory behavior of thin films, however; and the recursive genetic fitting algorithms can deal with the subtleties of the XRR and Pendellosung fringes. These algorithms are based on the Darwin method[29]. Whereas the Laue method treats the system as an idealized crystal, the Darwin method is a dynamical layer-based method that accounts for total scattering from all atomic layers. This method subdivides the system based on thickness and material properties then sequentially solves for total scattering from each plane from the bottom up. Additionally, the software incorporates incident angle and divergence correction and robust optimization.

All figures presented herein are separated into two groups. The first four samples (S1-S4) are referred to as the "thin" samples, while the later three (S5-S7) are "thick". The range of thickness for the thin samples is roughly 8-13nm, and the thick samples

range 20-23nm. There are distinct differences between these groups that will be used to compare the analysis results as well as for reinforcement of the validity of the interpretation of the unique aspects of these films. It will be evident that the samples peak widths are primarily thickness limited as discussed earlier. The symmetric survey scans presented immediately below, however, exhibit an increase in background signal for low angles. This is due to a wider horizontal receiving slit (beam height/integration width) for these measurements in order to attain an intensity high enough to analyze. Divergence from the beam in this direction does not negatively impact the resolution of the measurement because this dimension is orthogonal to the diffraction plane. Other than these first four scans, all other diffraction data ($2\theta/\omega$ coupled, ω rocking curve, φ survey) were collected using the optics listed in the table above.

Orientation and Crystallinity

Out of Plane θ/2θ-Survey

The $\theta/2\theta$ survey scans for the four thin samples are presented in Figure 12. The forbidden Si(002) and (006) peaks are apparent in every scan, but their presence is insignificant and will not be discussed further. There is clear agreement between the scans with regards to having a single phase of STO(00L) out-of-plane with a single strong substrate peak from the Si(004) diffraction. It is evident that the samples are oriented parallel with the Si as far as the out-of-plane conditions are concerned. Samples S1-S4 are 8.6nm, 13.2nm, 9.4nm, and 9.2nm respectively and there is a clear trend of increasing intensity with thickness as would be expected. From these wide angle scans there are hints of oscillations around the STO(002) peaks which, when zoomed in on and

clearly resolved, indicate a sharp interface and high crystallinity with little variation in the measured diffraction spacing. These fringes will be more clearly demonstrated in the coupled scan section later.

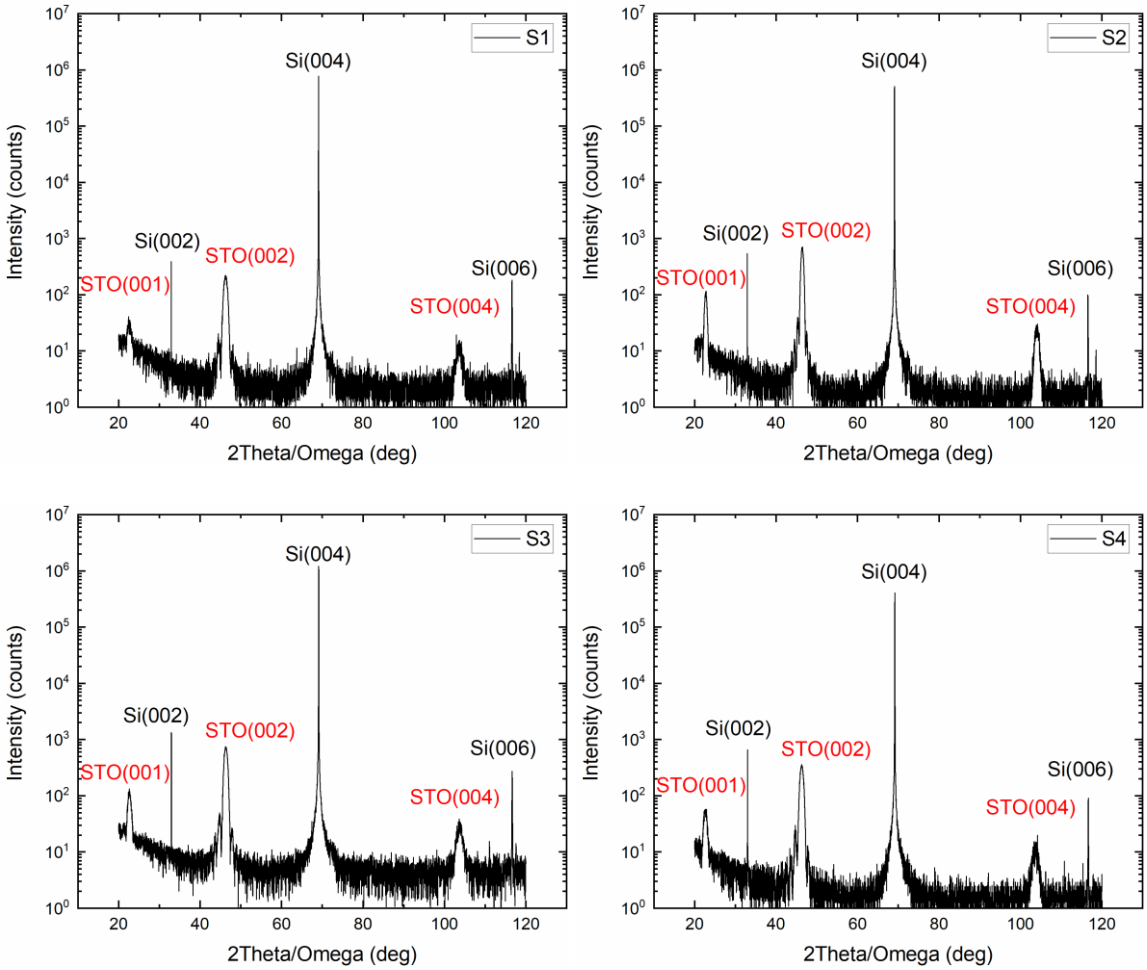

Figure 12: θ/2θ survey scans of S1 – S4 demonstrating single crystal phase and STO(00L) || Si(00L).

Similar to the thin samples, the thick samples (Figure 1) exhibit a single out-of-plane crystal phase oriented with the silicon substrate with notably higher intensity and fringes associated with the STO(001), (002), and (004) peaks. The emergence of the STO(003) peak for the thick samples is not evidence of anything in addition to the thin

samples, but simply that the diffraction has attained enough intensity to emerge from being hidden under the Si(004) background curve.

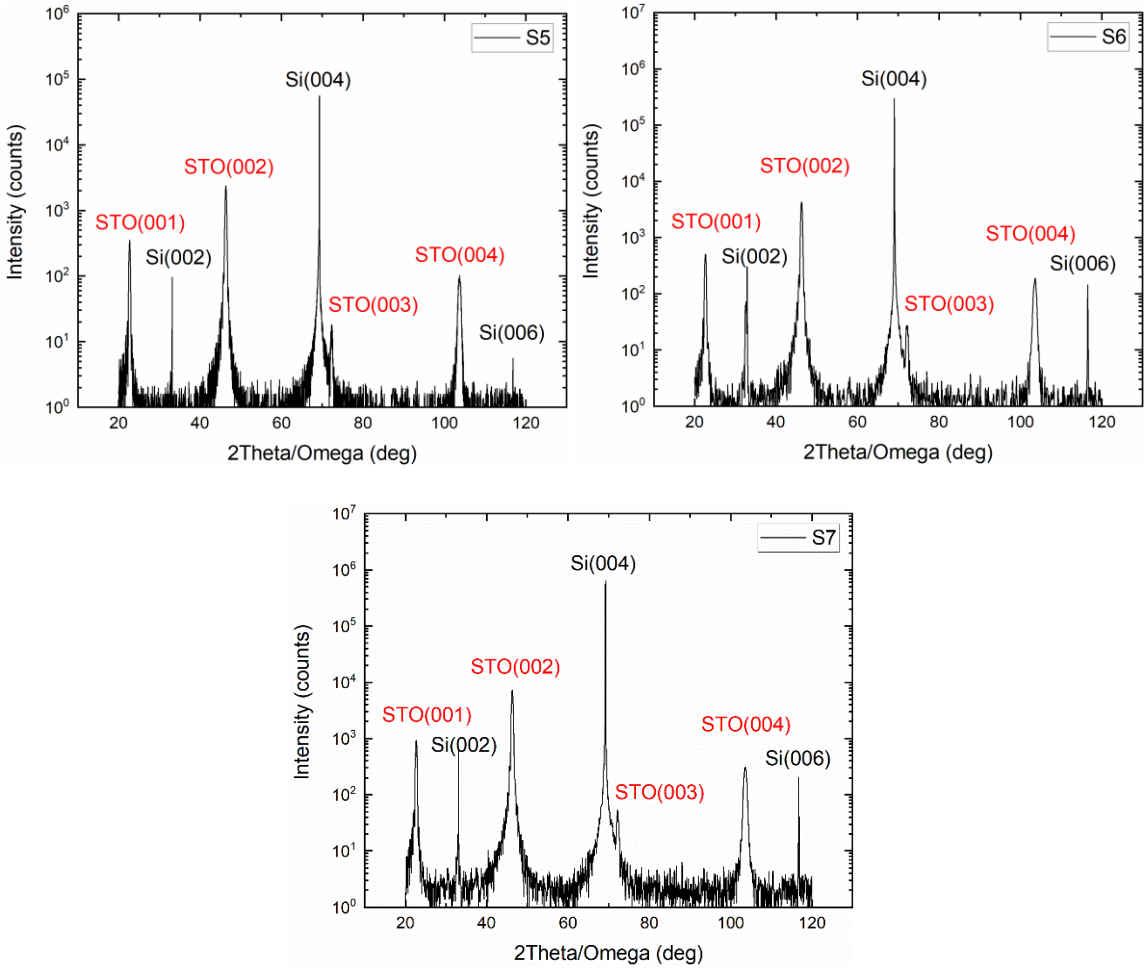

Figure 13: θ/2θ survey scans of S5 – S7 demonstrating single crystal phase and STO(00L) || Si(00L).

For all samples the angular difference between the STO(002) and Si(004) peaks with regards to goniometric tilt is less than 0.05°. This effectively demonstrates that there is no offcut or misalignment between these two planes and thus the c-axis orientation of both films is the same.

Asymmetric φ-Survey

There is no qualitative difference between the two groups for this measurement. The φ surveys of every sample exhibit strong cubic rotational symmetry; the only difference being that the thick samples had higher intensity, which is expected (Figures 14 & 15). Every sample exhibits 45° rotation with respect to Silicon and 90° degeneracy in φ. Originally the Si{202} and STO{202} families of planes were measured to find these relationships, but aberrant peaks that appeared to have the same quality as the forbidden Si(002) and (006) appeared in the STO data. The STO{103} family of planes has a better profile with no aberrant peaks.

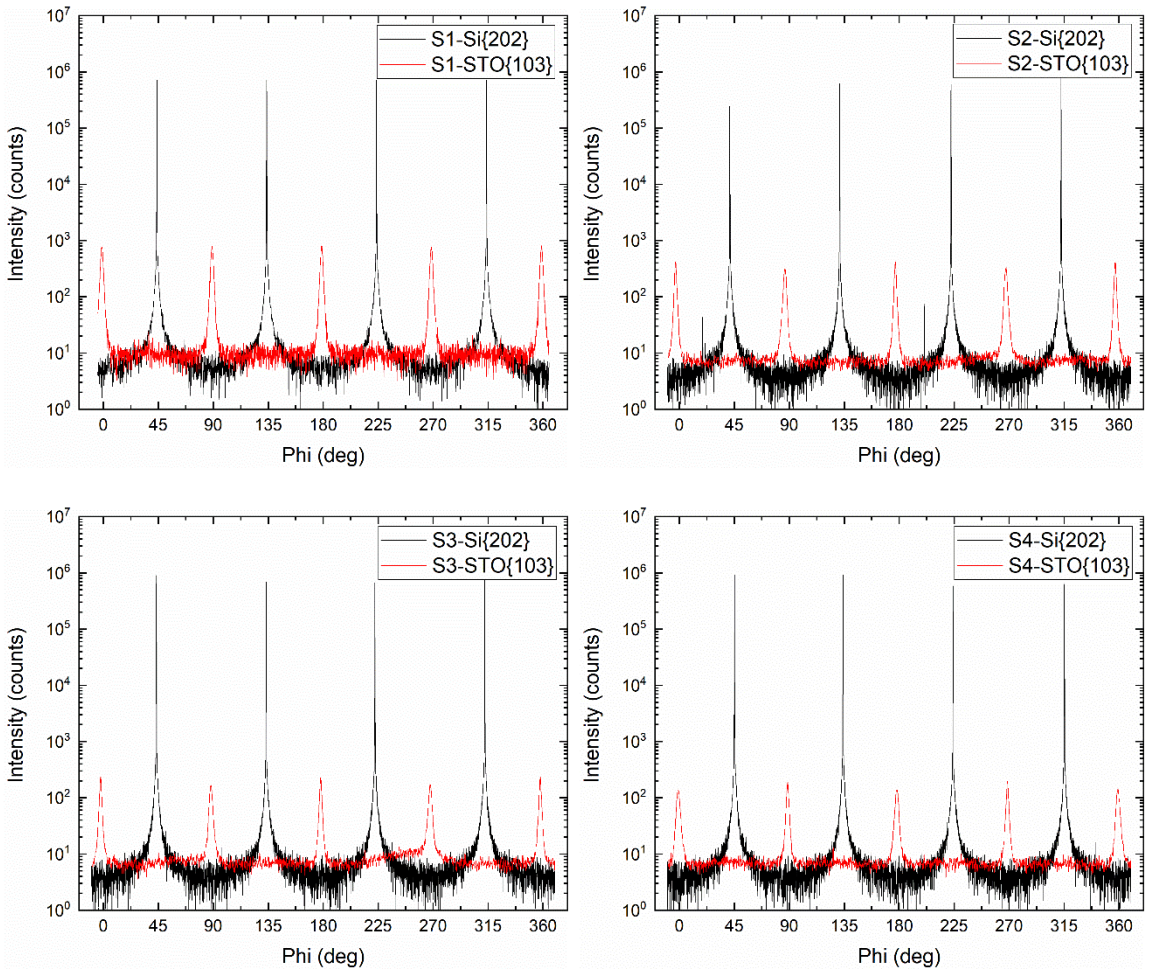

Figure 14: φ scans of S1 – S4 demonstrating single crystal phase STO(100) || Si(110).

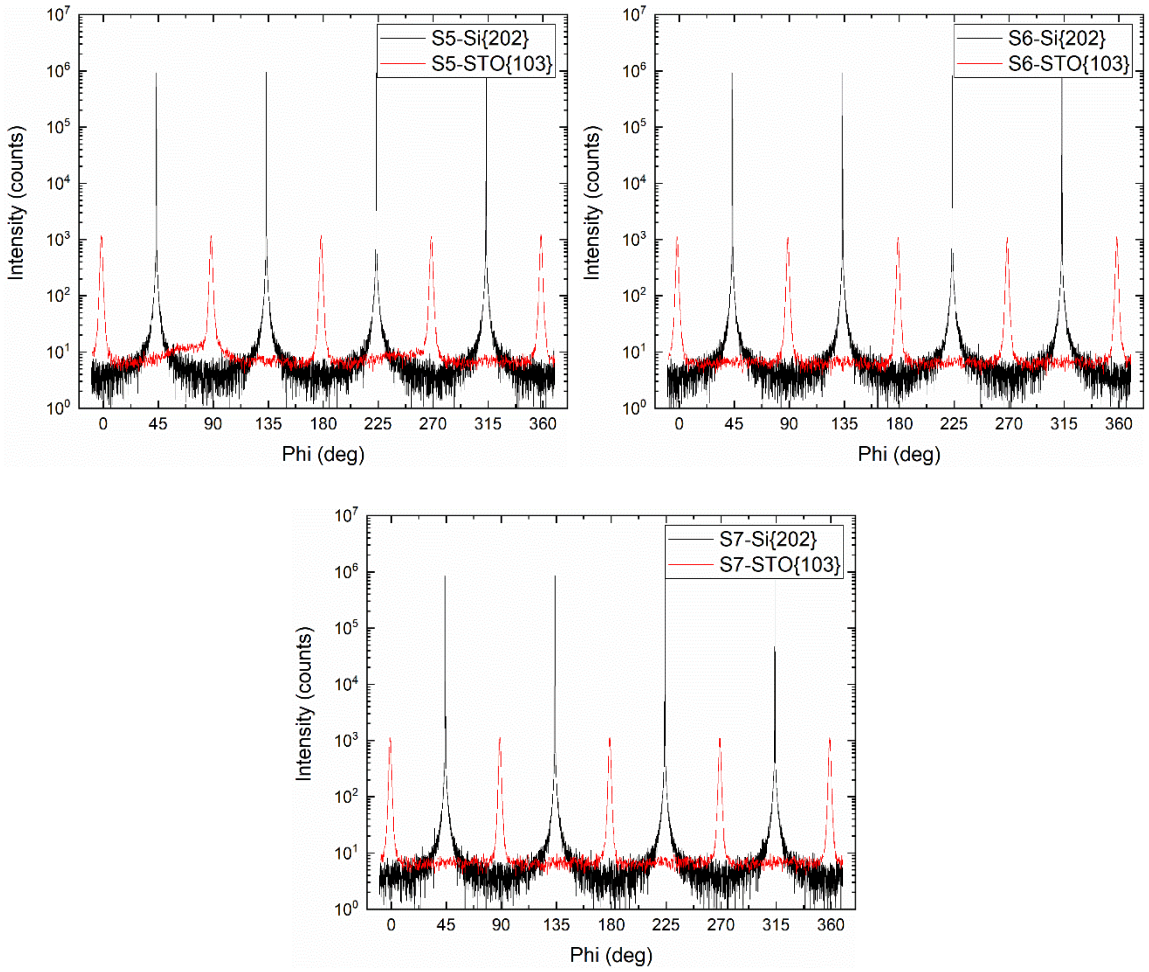

Figure 15: φ scans of S5 – S7 demonstrating single crystal phase STO(100) || Si(110).

Interface Interference Effects

XRR

XRR analysis for thin films is generally harder than that for thicker films due to a lack of oscillatory behavior to model. In general, the thicker the sample, the more Kiessig fringes there are, and the greater the density of features the easier it is for the recursive algorithms the software uses to find optimized parameters. The thin samples tend to be rather featureless except for a single oscillatory mode that models the overall

thickness of the film. These are presented in Figure 16 and model parameters in the table below.

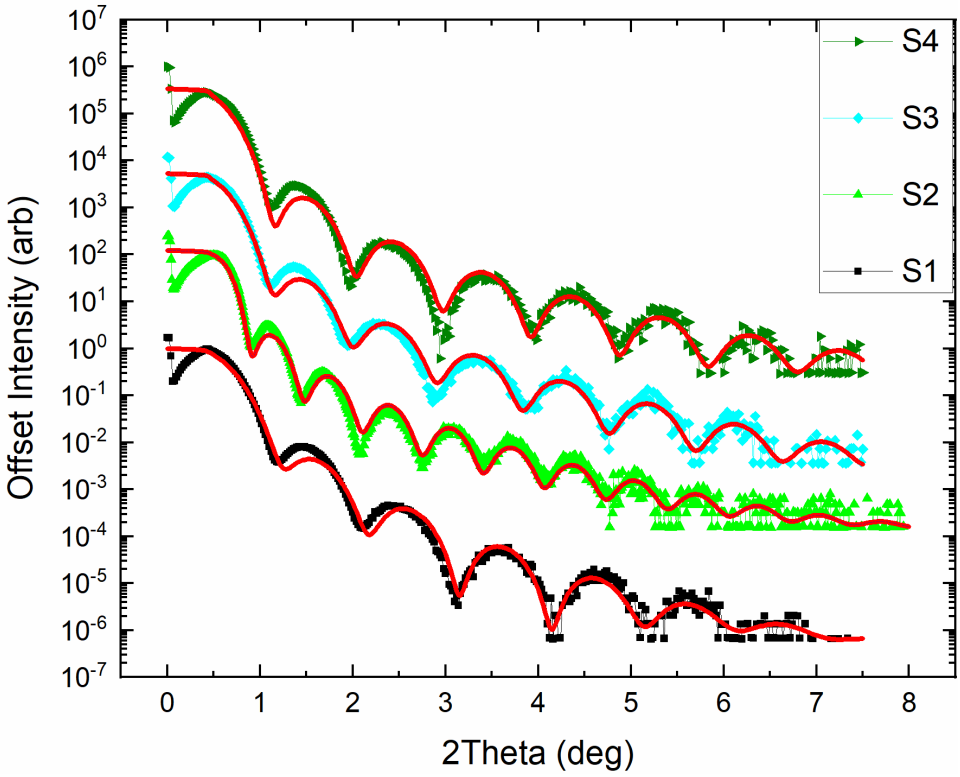

Figure 16: XRR profiles for S1 – S4 with single layer based fitted curves.

Table 3. Single Layer XRR			
	Thickness (nm)	Density (g/cm3)	Roughness (nm)
S1	8.638	6.4	0.521
S2	13.184	4.91	0.248
S3	9.366	5.6	0.282
S4	9.136	5	0.24

The thick films cannot be modeled with a single layer. The thick films XRR fittings are presented in Figure 17. They each exhibit a second thin, low-density layer that fits at the STO-air interface. This is not an uncommon feature of XRR curves. It is

thought that this is a layer of the film that is interacting with atmospheric conditions in the ambient environments of most laboratory diffractometers. In order to evaluate this, however, the samples would need to be measured under vacuum after being baked to dehydrate the surface. These subtle layers are not actually part of the crystal and are variable in subsequent measurements. It is generally accepted that this is the result of atmospheric water contamination and to model the system using this layer as a fitting aid, but not to include it in the overall thickness of the samples [30].

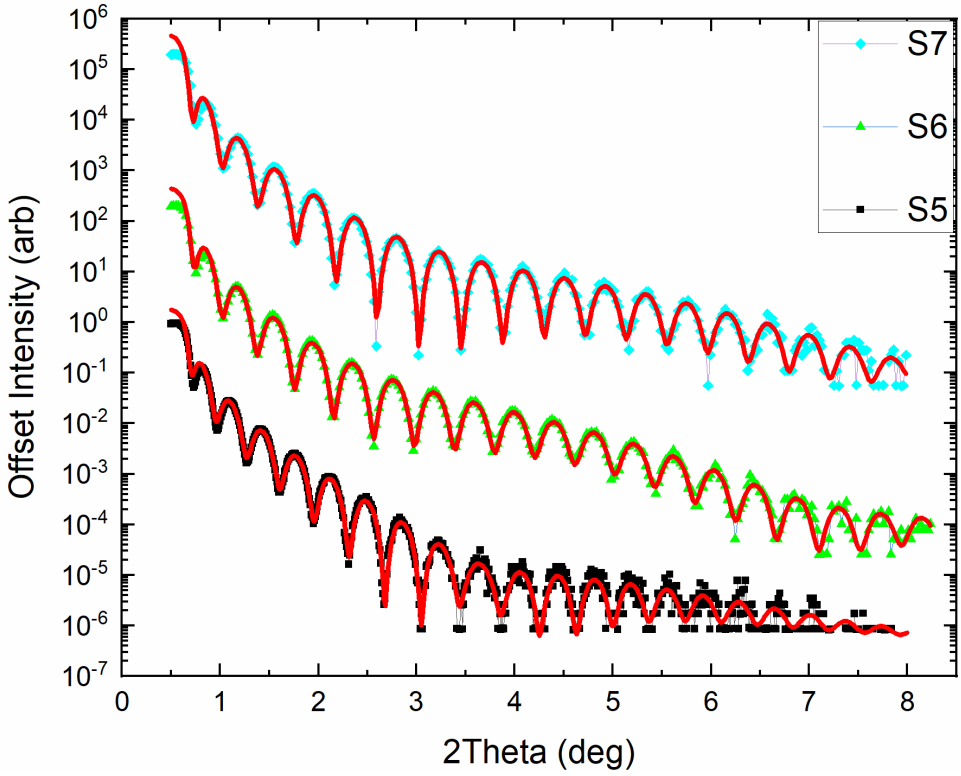

Figure 17: XRR profiles for S5 – S7 with fitted curves based on a single primary layer of STO with a thin low-density layer on top to improve fitting.

Returning to the thin samples, this low density "wet" layer does improve the fit without changing the overall thickness of the films (Figure 18). In reexamining the original single layer fitting there is a consistent mismatch between the first few minima

that doesn't affect the second fitting. It stands to reason that a surface effect would primarily affect these low angles where the penetration depth is the shallowest and refraction is dominant. Parameters for the double layer fitting for all samples are included in the table below.

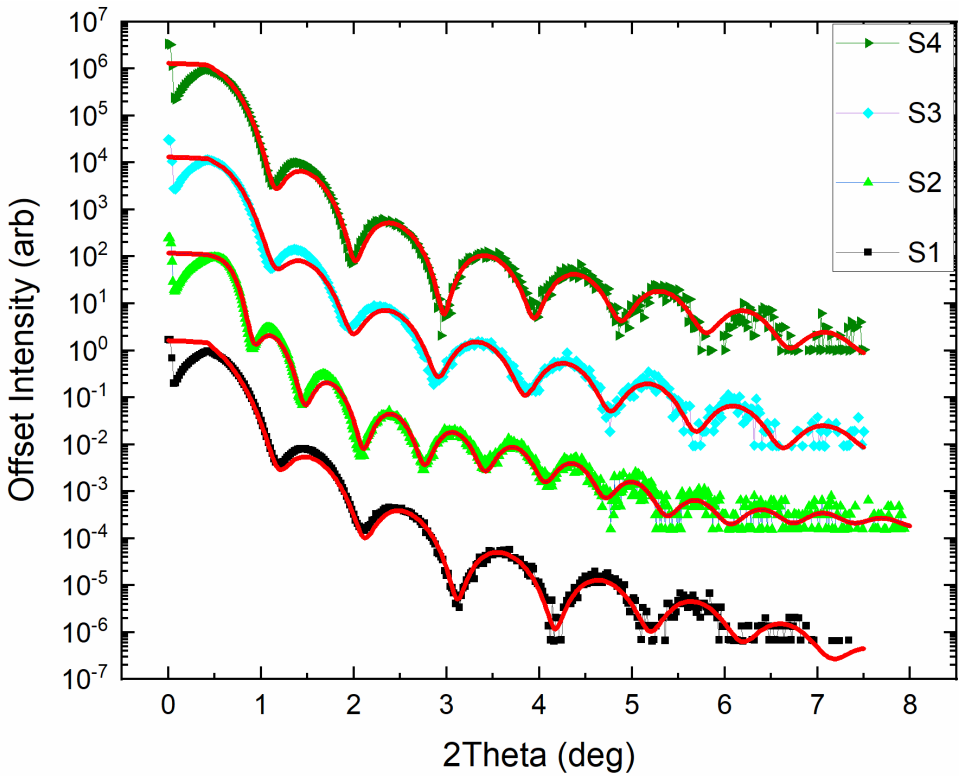

Figure 18: XRR profiles for S1 – S4 with fitted curves based on a single primary layer of STO with a thin low-density layer on top to improve fitting.

Table 4. Double Layer XRR

	Primary thickness (nm)	Density (g/cm3)	Roughness (nm)	Thickness of cap (nm)	Density (g/cm3)	Roughness (nm)
S1	8.6	5.4	0.36	1.34	0.84	0.2
S2	13.2	5.96	0.21	2.3	0.63	0
S3	9.4	6.3	0.285	1.872	0.48	0
S4	9.2	5.87	0.3	1.58	1.04	0
S5	23.3	4.88	0.37	1.312	1.43	0.2
S6	21.3	4.75	0.255	1.932	0.56	0.14
S7	20.8	4.34	0.272	1.57	0.83	0.21

XRR is sensitive to sharp interfaces and density contrast at those interfaces. Rough interfaces are handled readily as they damp the transmitted beam. The effect of subtle variation in the density is hard to discern. The best one can achieve is a generalized density distribution between two more well-defined interfaces (such as air and substrate interfaces). This is where the subtlety of modeling starts to come into play: the fit for the thin films as one layer worked for the most part, but a single layer model breaks down from the perspective of the 2θ/ω coupled scans and ω rocking curves that follow.

2θ/ω-Coupled Scan: Simple Treatment of Pendellosung Fringes

The analysis of Pendellosung or Laue fringes can be roughly done by modeling a single curve based on the Laue equation. This method will give you a rough estimate of film thickness and average relaxation but is not robust enough to account for the subtle variations from ideal conditions present in the following scans. Attempts were made to model the Laue equation in Origin using attenuation by an asymmetric offset peak, but none of these attempts improved on the single oscillatory fitting. These attempts at directly modeling to the theory failed and modeling was completed with the genetic fitting algorithms developed for this specific purpose by Rigaku. All successful data analysis of Pendellosung fringes was performed using Rigaku's GlobalFit software. The initial attempt to model both sets of films with single STO layers are presented in Figures 19 and 20 respectively.

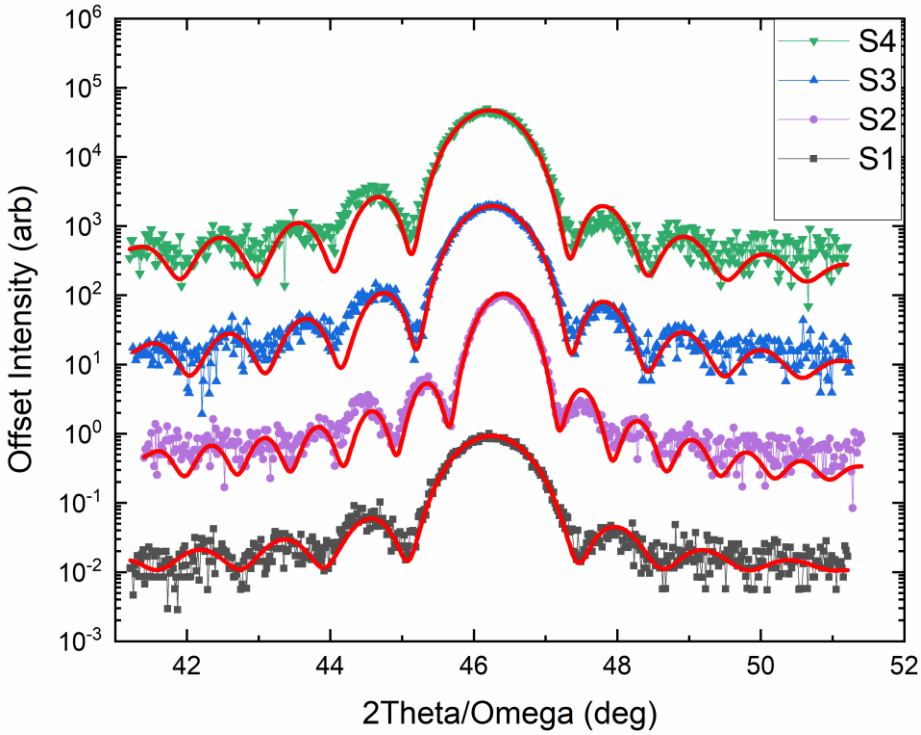

Figure 19: Single layer Pendellosung fittings for S1 – S4. Note the asymmetry on the either side of the measured peak.

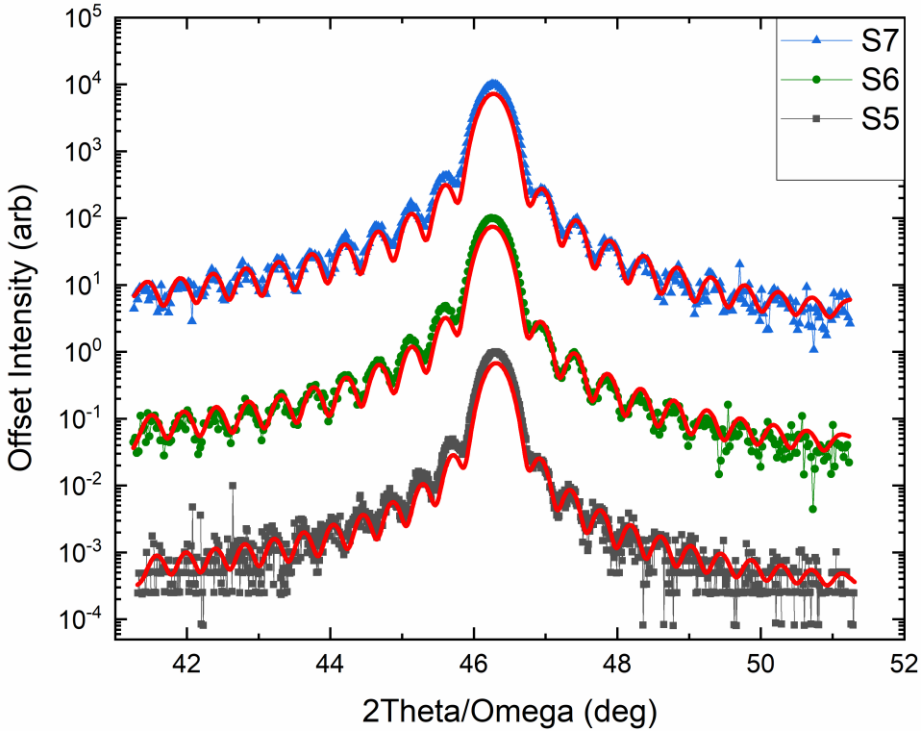

Figure 20: Single layer Pendellosung fittings for S5 – S7. The same asymmetry appears for these measurements.

It is important to note here that the differences presented between these initial attempts and the models we settle on are subtle. The differences evident when modeling on a computer monitor are not always apparent on a page sized graph, but certain features are apparent upon close examination. The thicknesses for the single layer Pendellosung fittings are consistent with those from XRR. These fitting results are presented in the table below. The results table for this and subsequent fittings contain the fitted thickness for the layers and a relaxation percentage defined as

$$\epsilon_{inp} = (1 - R)(a_{ref} - a)/a,$$

Where ϵ_{inp} is the in-plane strain, R is the fractional lattice relaxation, a_{ref} is $|Si(110)|/\sqrt{2}$ = 3.8402Å, and $a\ is\ |STO(100)|$ = 3.905Å. This equation describes how much the in-plan lattice parameter conforms to the substrate: 0% is coherence and 100% is full relaxation.

The first and most obvious misfit in these models is the clear asymmetry around the main peak with amplification of the intensity on the left-hand side. This was the motivation for attempting the convoluted fitting with Origin. It is a characteristic of highly strained films to exhibit asymmetry in diffraction profiles. Asymmetry to higher angles evidences tensile distortion in-plane and compression out-of-plane. What we see here, asymmetry to lower angle, would be associated with compression in-plane and tensile distortion out of plane.

The distortion detailed by asymmetry in a regular fitting peak tends to be distributed in the film and shows up as a weak attenuation to the Pendellosung fringes. This is not what appears in these measurements. There is an amplification greater than that provided by an asymmetric peak fitting. This is something that appears for

superlattices and heteroepitaxial films with thin buried interface layers [30]. This asymmetry will be addressed later with consideration of the results from the following analysis on rocking curves.

Table 5. Single Layer Pendellosung Model		
Sample	Thickness (nm)	R% Avg
S1	8.12	60
S2	12.82	90
S3	9	62
S4	8.8	54
S5	23.13	69
S6	21.01	60
S7	20.71	62

Pseudomorphic Growth and Coherent Strain

ω-Rocking Curves

The rocking curves of S2-S4 exhibit very sharp central peaks superimposed on a diffuse background curve which resembles a normal rocking curve for films this thin. This sharp central peak is evidence of two distinct regions in the STO. It will be shown that this peak is associated with a highly crystalline coherent layer at the STO/Si interface. The rocking curves with fitted peaks are presented in Figure 21.

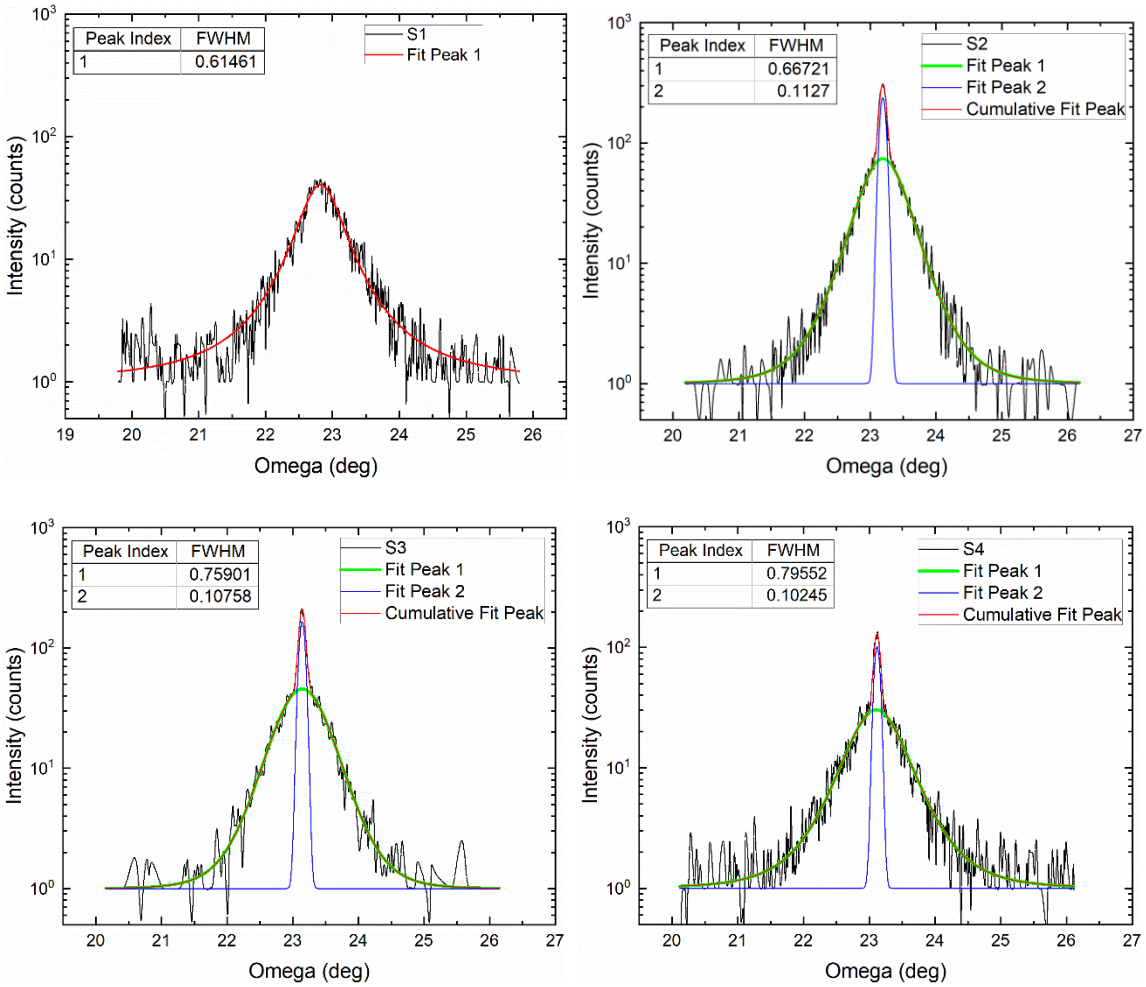

Figure 21: Rocking curves for S1 – S4 for which S2 – S4 exhibit sharp central peaks associated with coherent layers at the STO/Si interface.

It is not immediately clear that the peaks for the thicker films should exhibit similar behavior. However, attempts to fit the thick films with a single peak failed to accommodate the background and tails of the profile; these fittings are presented in Figure 22.

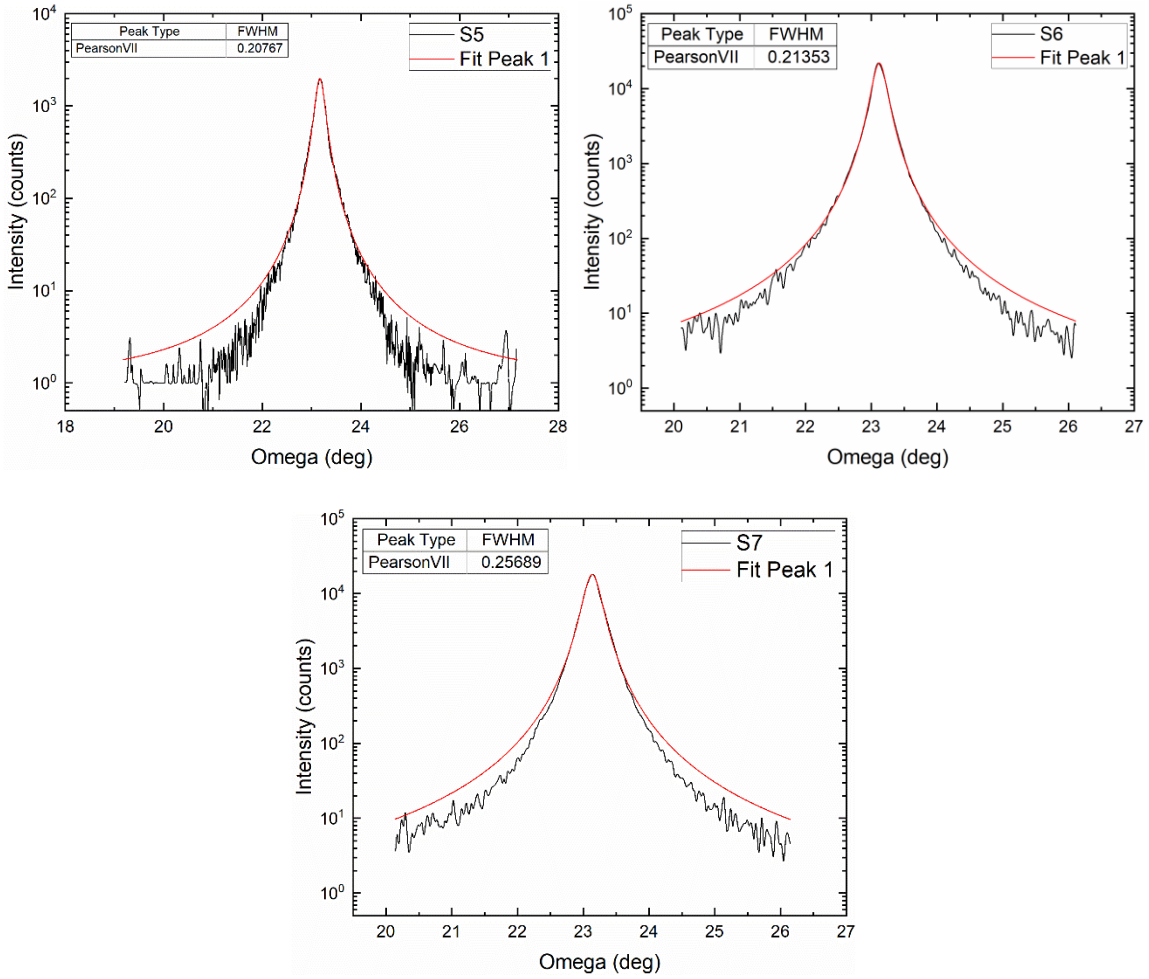

Figure 22: Single function peak fitting of thick films that fail to account for all features.

Instead it appears that this central peak persists, and if the best fits for the thickest films are considered, this peak remains part of the system (Figure 23). The diffuse peak changes according to expectations as to how a thin film relaxes as it gets thicker: the intensity increases and the width narrows. It would seem reasonable that the sharp central peak, being associated with a buried layer, would be suppressed as the films get thicker and relaxation of the cap layer was accommodated by an increase of dislocations at the interface. This suppression of an interfacial strained layer by the dominance of the relaxing layer on top does not appear to be happening here.

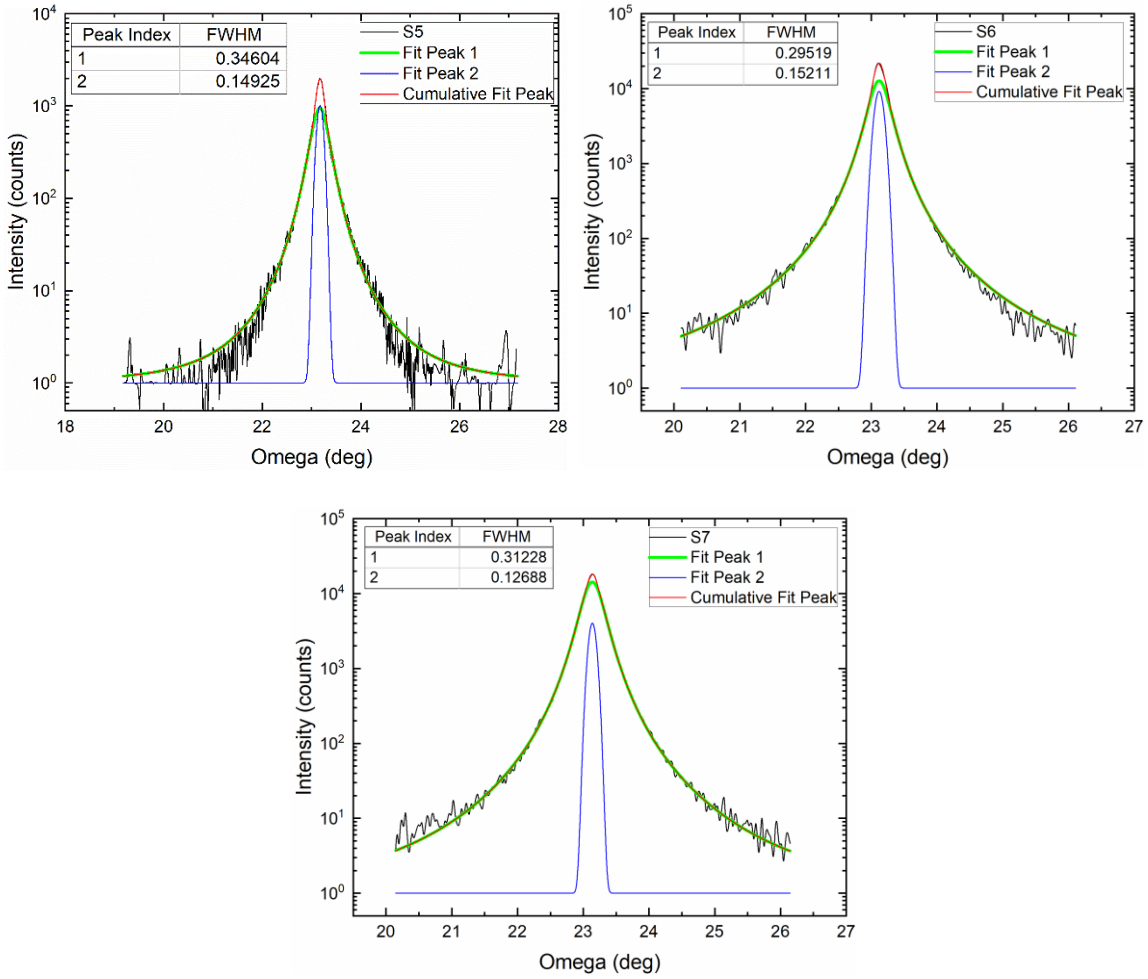

Figure 23: A similar model to the sharp central peaks fromS2 – S4 is necessary for successful fit of S5 – S7.

Critical Thickness

When an epitaxial layer is grown on a substrate with a mismatch that is not too large (~1%) coherent growth can take place. This means that the mismatch is compensated in the epitaxial layer by elastic relaxation without the formation of defects. This is called pseudomorphic growth. For a cubic, biaxially strained pseudomorphic layer relaxing according to Poisson's ratio the elastic energy density is given by

$$\frac{E}{At_L} = 2G\varepsilon_{||}^2 \frac{1-\nu}{1-\nu},$$

Where A is the interfacial area, t_L is the strained layer thickness, G is the shear modulus, $\varepsilon_{||}$ is the in-plane strain parallel to the interface, and ν is Poisson's ration for the layer material. This describes a system accumulating strain energy as the layer thickness increases and at some critical thickness the system will have built up enough energy to form structural defects that plastically relax the strain through various dislocation mechanisms[31].

The amplitude and narrow peak width of the coherent layer is similar to a principle of diffraction for perfect crystals called the Borrmann effect. The Borrmann effect is the observed anomalous decrease in the absorption of x-rays and a commensurate increase in the intensity of diffraction when the Bragg condition is met for nearly perfect crystals[30]. At the Bragg condition there is total constructive interference from all possible scattering sites from within the area illuminated by the x-ray beam. A diagram illustrating this is shown in Figure 24.

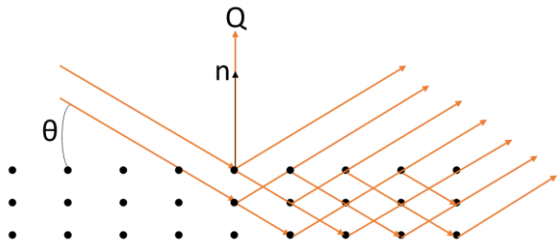

Figure 24: Diagram of the Borrmann effect.

In the samples presented here, the conditions are not such that this is indeed the Bormann effect. This effect is associated with large perfect crystals measured in transmission geometries where the crystal appears opaque to x-rays except at exact Bragg conditions where transmission and diffraction are amplified. These films are not opaque

to x-rays, nor are the measurements taken in transmission mode. Nevertheless, there is an associated amplification of diffraction intensity associated with a peak with a full width half max much narrower than expected for a film undergoing any type of relaxation.

This is how the coherent layer can be confirmed: evidence that the layer is uniform and highly crystalline. Since the average properties of the rest of the film do not exhibit this level of crystallinity, the presence of this type of peak is evidence of strong influence from the substrate. There must be coupling in which the increase of crystallinity in the film is due to conforming with the near perfect substrate.

Robust Treatment of Pendellosung Fringes

Considering the clear indication that a persistent coherently strained layer exists at the STO/Si interface, the 2θ/ω coupled scans were reexamined in GlobalFit including a coherently strained interface layer (Figure 25). Adding the coherently strained layer at the interface appears to relieve the burden of fitting the entire film as having the same relaxation (constant c). These curves are shown in Figures 26 and 27 for thin and thick sample groups respectively.

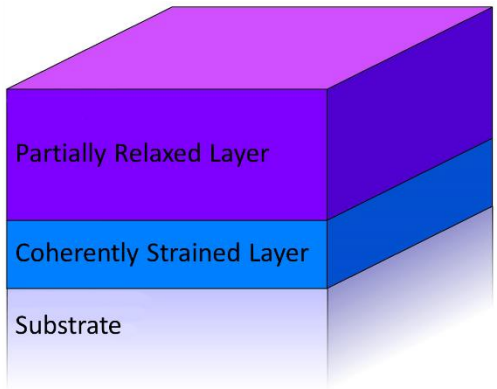

Figure 25: Double layer structure model with coherent layer at the ineterface.

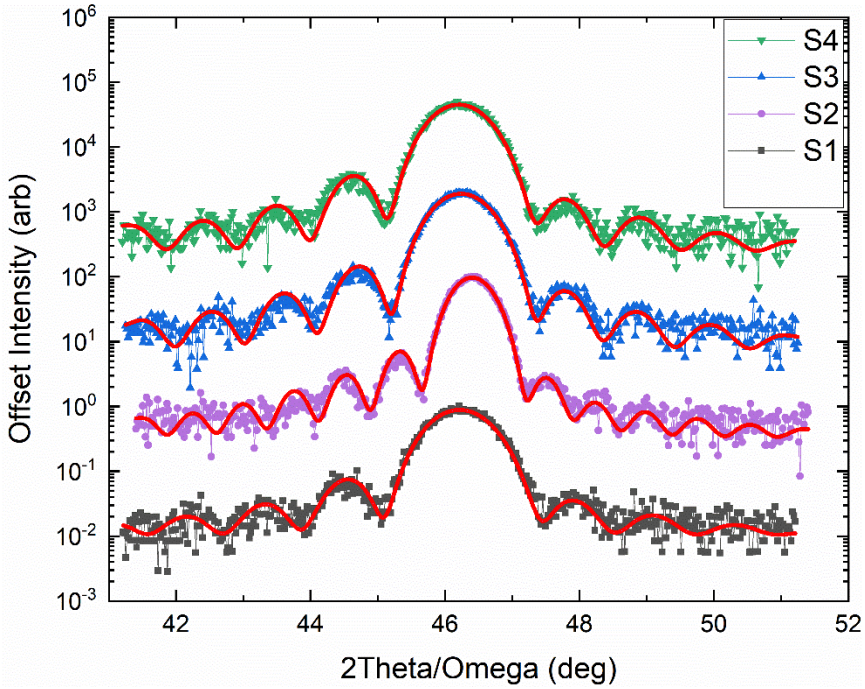

Figure 26: Double layer Pendellosung fittings for S1 – S4. The asymmetry observed for the single layer fitting is gone.

In most cases the top layer will settle at a slightly higher relaxation than when modeled as a single layer. This universally improved the fitting with respect to the asymmetry that coupling the Laue equation with an asymmetry peak was not able to account for. Looking at the fitted curve for the coherent layer in the absence of the top layer reveals that instead of simply skewing the fitting to lower angles by amplification from the intense central peak the additional interference of the first order minima on the high angle side attenuates the fitting and together these account for the strong asymmetry. Fitting values for this model are presented in the table below.

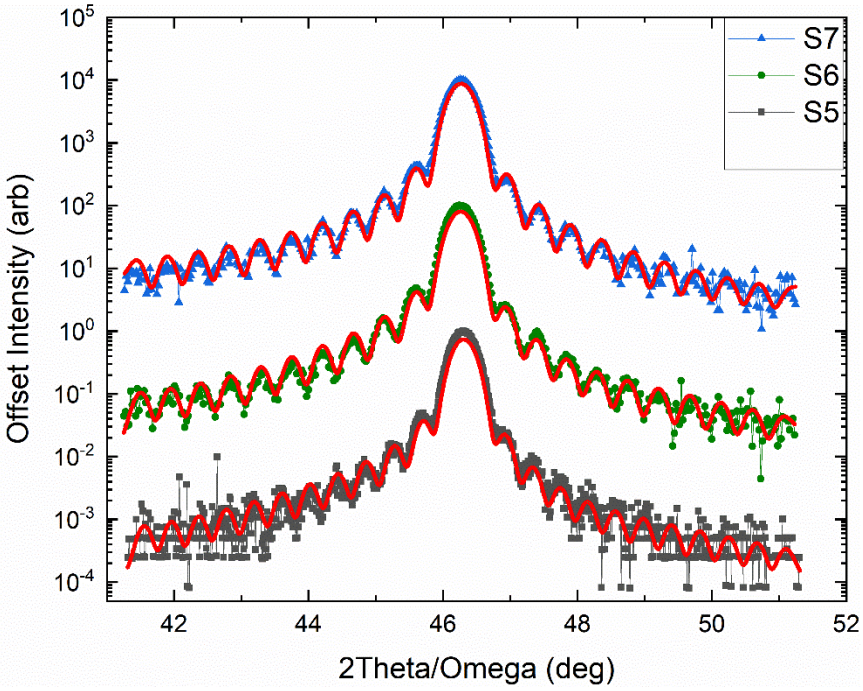

Figure 27: Double layer Pendellosung fittings for S5 – S7. The asymmetry is mostly improved by this fitting.

Table 6. Double Layer Pendellosung Model

Sample	Coherent Interface thickness (nm)	Relaxed Layer thickness (nm)	R% (Relaxed)	#ML (Coh)	Total Thickness (nm)
S1	2.5	5.69	70	6.3	8.19
S2	2.17	10.56	95	5.5	12.73
S3	2.34	6.66	70	5.9	9
S4	2.83	5.91	69	7.2	8.74
S5	2.14	21.02	70	5.4	23.16
S6	2.31	18.76	62	5.9	21.07
S7	0.93	19.79	62	2.4	20.72

In samples S6 and S7 modeled with two layers, the coherent layer and relaxed layer seem to be competing due to a lack of a relaxation gradient. The relaxed layer fit to higher angles for S6 causing a slight offset from the main peak and overcompensation in

thickness by the coherent layer. For S7 the relaxed layer fit to lower angles to make up for a lack of relaxation which caused slight asymmetry in the oscillatory tails. This led to a slight offset in the main peak position as well.

Further refinement of the model with an intermediate, partially relaxed layer between the coherent layer and a relaxed cap layer (Figure 28) was introduced and the goodness of fit was minimized (Figures 29 & 30). The thin samples do not benefit from the addition of the cap layer and the results are not significantly different for the thickness of the coherent layer. The triple layer models for S6 and S7 are the best fits with the minimum number of layers and are the only fittings that produce most of the features in all the curves. The results for this fitting for all samples are reported in the table on the next page.

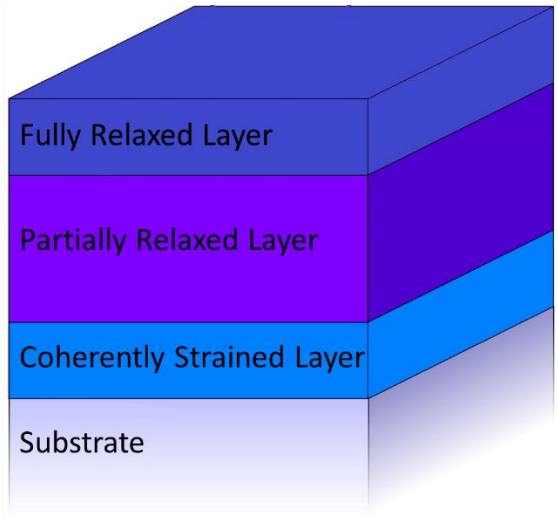

Figure 28: Triple layer structure model with coherent layer at the interface and a fully relaxed cap layer.

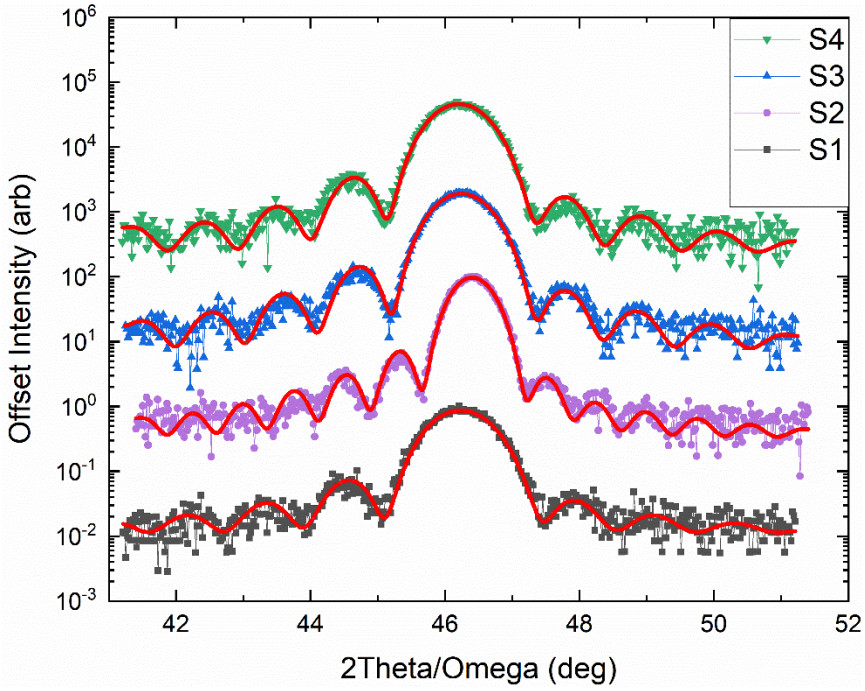

Figure 29: Triple layer Pendellosung fittings for S1 – S4. The addition of the cap layer does not substantial change the fitting results for these samples.

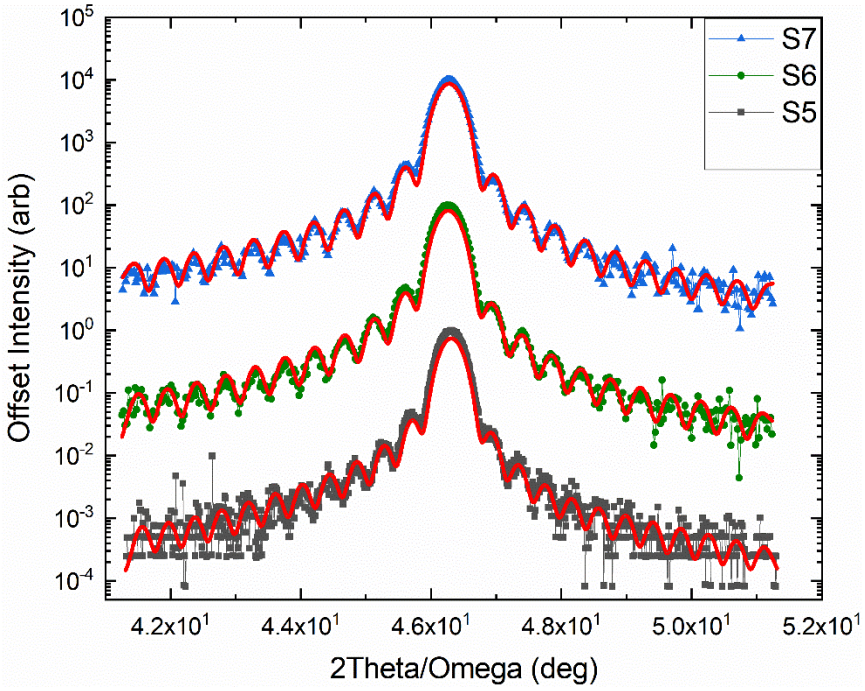

Figure 30: Triple layer Pendellosung fittings for S5 – S7. It is necessary to include the cap layer for these thick films to achieve the best fit.

Table 7. Triple Layer Pendellosung Model						
Sample	Coherent Interface thickness (nm)	Relaxed Layer thickness (nm)	Cap thick (nm)	R% (Relaxed)	#ML (Coh)	Total Thickness (nm)
S1	2.24	5.7	0.28	70	5.7	8.22
S2	2.17	11	0	95	5.5	13.17
S3	2.33	6.14	0.5	70	5.9	8.97
S4	2.67	4.9	1.2	65	6.8	8.77
S5	2.13	20	1	70	5.4	23.13
S6	1.94	18.24	0.89	61	4.9	21.07
S7	1.52	18.1	1.1	63	3.9	20.72

The two claims that the sharp central peak of the rocking curves directly indicate a coherent layer at the interface while also using subtle variation in the coupled scans to say the same thing seem to be at odds. Two distinct peaks are not observed in the coupled scans due to the dominance of the interference in the Pendellosung oscillations. The broad central peak and long Pendellosung oscillation tails essentially hide the lower intensity peak associated with the coherent layer as a modulation to the interference pattern. The fact that the coupled scan peak is much broader than the rocking curve and the scan is probing a varying lattice spacing means that the averaging capable in the Bragg reflection can compensate for this change in lattice constant. The rocking curve simply cannot accommodate this, and since the Bragg condition is held constant at the average lattice spacing, any deviation away will be more sensitive to highly crystalline layers and attenuate rapidly when tilting away.

Again, the effect on the coupled scan can be differentiated from peak asymmetry and broadening due to compressive strain. This is determined by the failure of any common peak fitting (Voight, PVII, Gaussian, Lorentzian) to accommodate this

asymmetry. An additional very thin layer with 0% relaxation placed at the interface does accommodate this, and it does so with the least parameterization to the system. It is not simple strain, but it is a simple fitting.

The reason we cannot distinguish these two regions in XRR is because they do not have a sharp interface with respect to the electron density contrast. This is necessary for XRR as it relies on refraction between surfaces to determine density and roughness. What XRR determines from a composition like that in our samples resembles a density distribution similar to that of a regularly relaxing film. We expect this as the presence of a refractory interface between the coherent layer and the relaxing layer would indicate a change in composition greater than any slight difference in stoichiometry one might expect from the presence of oxygen vacancies.

Determination of Lattice Parameters

θ/2θ-Survey

After determining the presence of a coherent layer for the thin samples, and the possible presence of a coherent layer in the thick samples, we wanted to determine the average value of the lattice parameters for the films and investigate the residual strain in the rest of each film above the coherent layer. This turned into an investigation into the average value of these parameters for the whole film, as it became clear that for films this thin differentiation of the coherent layer from the rest of the film is very difficult outside of rocking curve measurements.

The following fittings in Figure 31 were performed to get a good fit for the out of plane lattice constant using the STO{00L} family of planes. The left-hand fitting is

deceiving; it appears to be a rather good fit of the peak index versus the reciprocal spacing. This is based on the Bragg equation and the slope would give an average value of the c parameter. The problem for this fitting is the sensitivity to the error in determining the peak position, and the slope is unreliable. This is evidenced by the appearance of a good fit with lines for all the samples lying directly on top of each other. These lines have different slopes and give different values for the lattice constant, all larger than the value determined directly from each peak.

The right-hand fitting is often referred to as the Nelson-Riley function [32] and is commonly used to determine the correct out-of-plane lattice constant [33]. This extrapolation relates the measured lattice parameter to the correct value by the following:

$$C_{measured} = K\left(\frac{cos^2\theta}{sin\theta} + \frac{cos^2\theta}{\theta}\right) + C_{correct}$$

Where K is determined by goniometric errors, and the expression in parentheses is a correction factor that takes into account peak shift due to absorption, refraction, and other optical effects. The intercept of $C_{measured}\ vs\ \left(\frac{cos^2\theta}{sin\theta} + \frac{cos^2\theta}{\theta}\right)$ gives more accurate values for the c parameter which are used in combination with asymmetric coupled scans from the next section to calculate the average in-plane lattice constant.

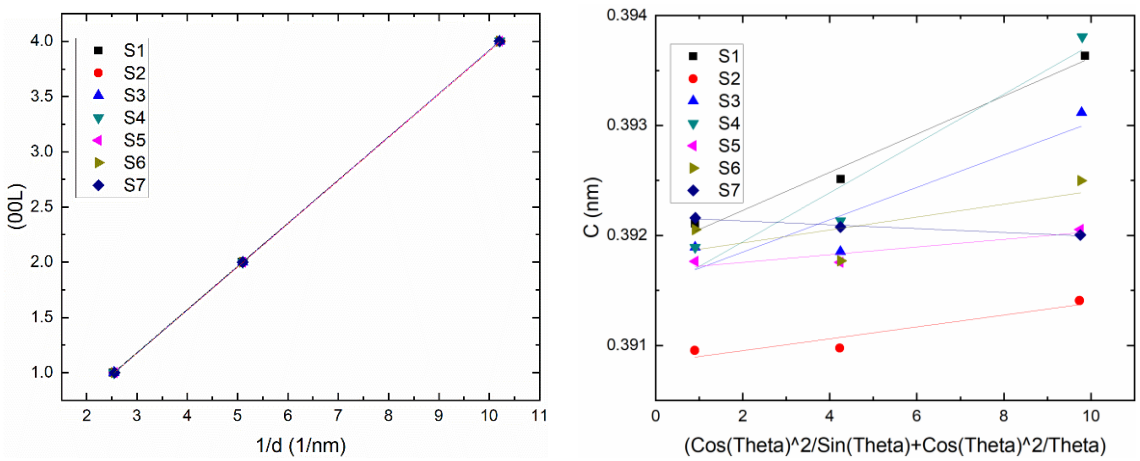

Figure 31: Left - Linear fit of the peak index vs reciprocal spacing for the (00L) peaks. Right - Linear fit for out-of-plane lattice parameter correcting for peak shift due to incident angle.

Asymmetric 2θ/ω-Coupled Scans

Figure 32 shows characteristic examples of the multitude of asymmetric peaks taken for asymmetric planes in order to get multiple points for the calculation of the in-plane lattice constant.

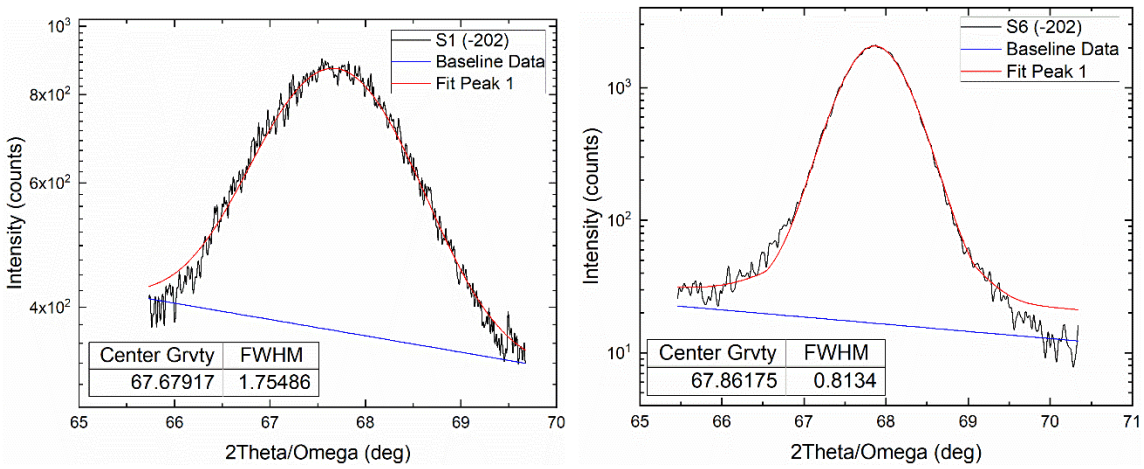

Figure 32: Examples of coupled scans for one member of the STO{022} family of planes for each group.

IV. DISCUSSION

Lattice Parameters

The calculated out-of-plane lattice constants c and in-plane lattice constants a determined from the {022} asymmetric peaks are plotted vs thickness on Figure 33. All films have an expanded c lattice constant as expected for the compressive strain at the interface. While for films S1-S4 the error in calculating c is large, films S5-S7 show a clear out-of-plane expansion. The in-plane lattice constants for S1-S4 also seems to be increased although the error bar is large. The large error for films S1-S4 stems from the low intensity of the diffraction peaks due to thickness. In contrast, the in-plane lattice constants for films S5-S7 are clearly decreased from the bulk value and track the increase in *c*. This is in agreement with the effect of strain on the lattice for the STO/Si heterostructure. Additionally, *c* and *a* decrease and increase respectively with the film thickness indicating that the film strain is relaxing with thickness. In this thickness regime, the degree of strain relaxation was reported to be strongly dependent on the film thickness [34].

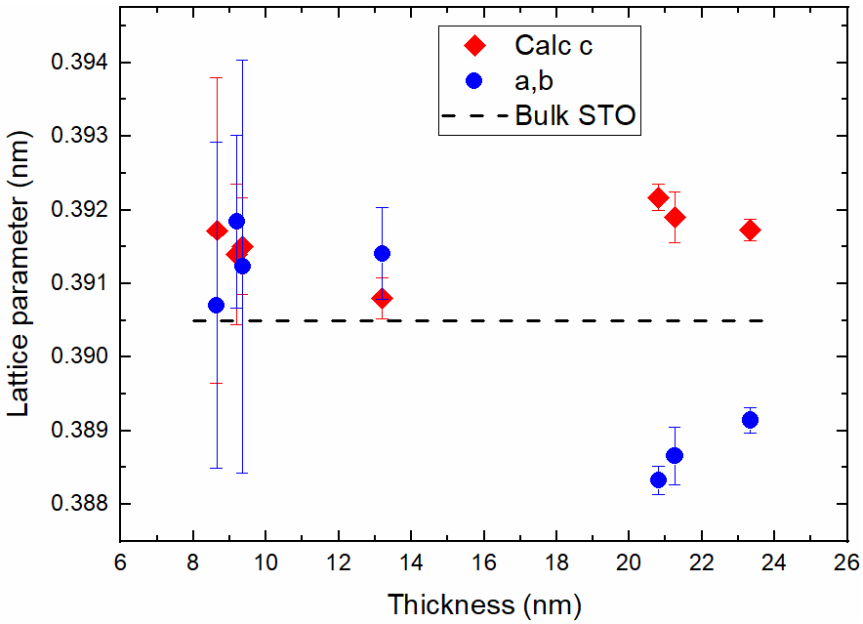

Figure 33: Lattice parameters vs. sample thickness based on XRR measurements.

The possible in-plane expansion of films S1-S4 may be due to the thermal expansion coefficient mismatch between STO and Si during the cool-down process [16]. The lattice parameter of STO films is also sensitive to the cation stoichiometry; nonstoichiometric STO films have a lattice parameter that is larger than that of stoichiometric STO at room temperature, independent of whether films are Sr-rich or Ti-rich [35]. The fact that *a* is clearly decreased from the bulk value for films S5-S7 ensures that stoichiometry was retained during the MBE growth of these samples as RHEED also showed. Note that S5-S7 were grown 3 years after S1-S4 when our group had further refined the challenging growth of STO on Si. Achieving accurate carrier density control in complex oxide thin films is especially difficult for crystal growth far from equilibrium such as Pulsed Layer Deposition where a Sr/Ti ratio change of 1% is sufficient to change the effective carrier density by orders of magnitude [36]. For oxide MBE growth, predefined oxygen deficiency levels require accurate, simultaneous control of Oxygen

pressure and deposition rate in addition to the control of oxidation rates of Sr [37] and Ti source materials [38].

Figure 34 shows the dependence of *a* and *c* on the partial Oxygen pressure during growth. The general trend is that strain is retained for growth under low Oxygen pressure for thicker films. It seems that PO2 influences strain more than film thickness. It has been shown that increasing the Oxygen pressure from 5 10^{-7} to 10^{-5} Torr during post-growth annealing (at 650 C for 30 mins) for 6 nm thick STO/Si films has the same effect seen here on *a* and *c*, relaxing the strain with *a* and *c* reaching bulk values at 10^{-5} Torr [39].

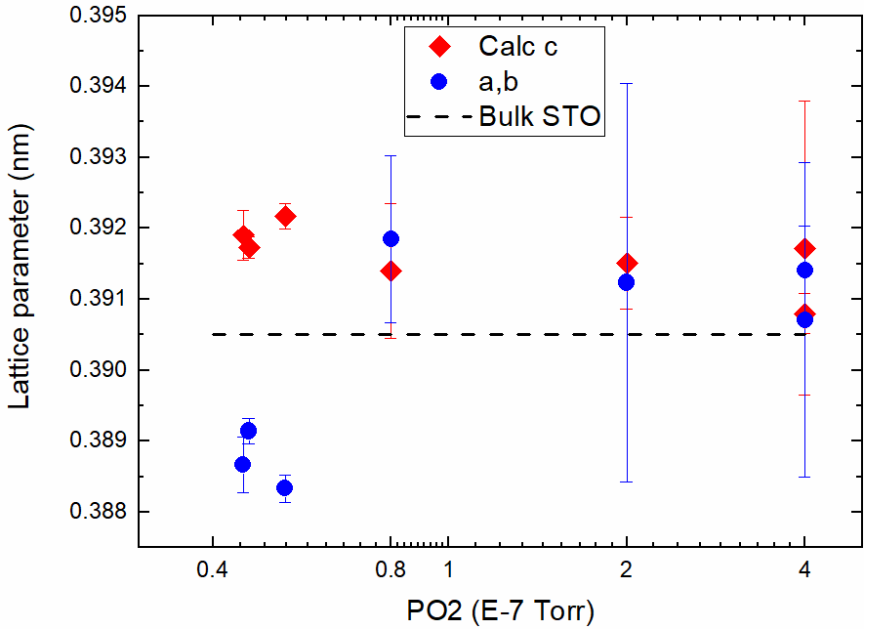

Figure 34: Lattice parameters vs. Oxygen partial pressure during MBE growth.

The FWHM of the STO (002) peak in the coupled 2θ–ω scans decreases with increasing film thickness as shown on Figure 35 and is equal to the calculated ideal broadening due to thickness (Scherrer formula with the Scherrer constant K=0.92). It had a minimum value of Δ(2θ) of ~0.4° for the thickest films.

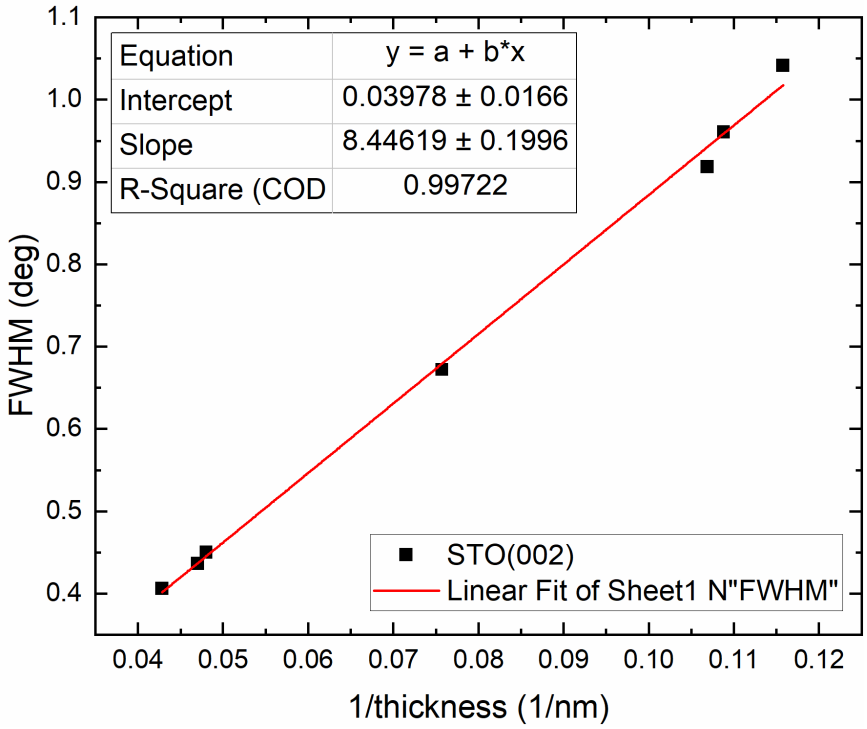

Figure 35: STO(002) FWHM vs. inverse thickness to determine Scherrer dependency.

Coherent Layer Growth

The ω rocking curves around the STO (002) reflection are plotted for film S1-S4 on Figure 36. The intense and narrow central peak with a FWHM of ~0.107° for films S2-S4 on top of a broader background indicates that the first few ML of $SrTiO_3$ are coherently strained and commensurate to Si as discussed earlier. It should be noted that S1 does not exhibit this characteristic peak, evidencing a lack of a persistent coherently strained interfacial layer. This is also reflected in the electrical results shown later.

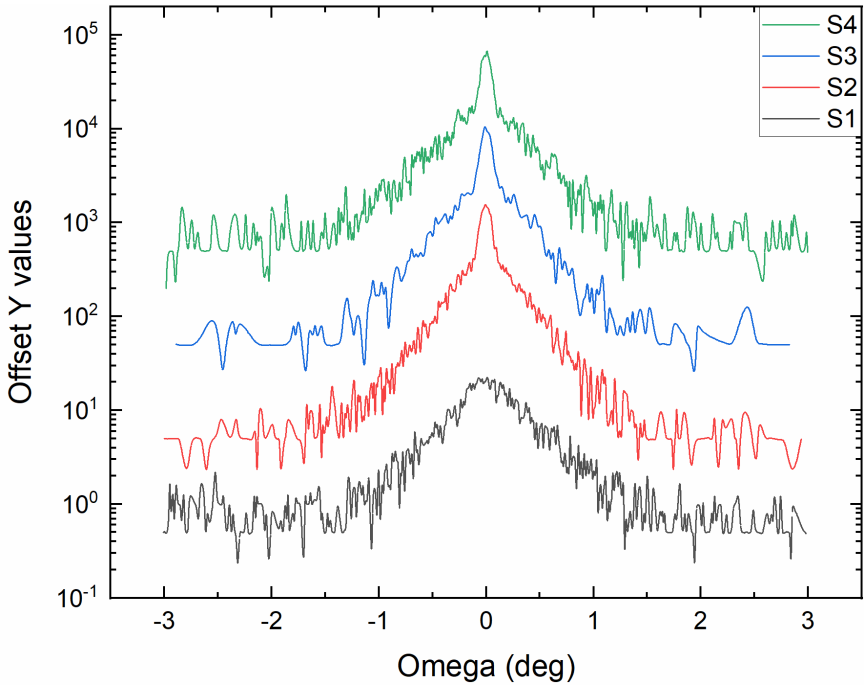

Figure 36: Rocking curve comparison for S1 - S4.

Below the critical thickness of ~ 2 nm, STO grows on Si coherently [12]. As thickness increases, the lattice relaxes to the bulk STO crystal structure through misfit dislocations. For a coherent layer to persist to thicker overall film values, the onset of relaxation must begin above the coherent layer. The relaxation mechanism is sensitive to the exact growth procedure with a critical overall film thickness (not the coherent layer thickness) of ~9 nm for high PO_2 and ~14 nm for low PO_2 [12] [17].

The broader central peak of film S1 indicates that the interfacial layer is not commensurately strained with Si and that strain is relaxing more gradually starting from the first few ML, possibly due to different growth parameters [19]. For sample S2-S4, the relative intensity of the peak with respect to the background represents the fraction of the film commensurate to Si(001) and is roughly the same for these three films. The sharp rocking curves peaks have a FWHM of ~0.107° indicating that these films have the same coherency thickness. This is in agreement with the 2- 2.5 nm thickness of the coherent

layer extracted from modeling the Pendellosung fringes thus confirming that S2-S4 are commensurate to Si by the same number of MLs.

Electronic Properties

We have used magnetotransport measurements to investigate the electronic properties of S1-S4. The sheet resistance of all samples increases as the temperature is lowered (Figure 37a). The conductivity (Figure 37b) is logarithmic in temperature, characteristic of 2d quantum corrections with a positive EEI contribution to the conductivity favoring parallel spin alignment. The spin-exchange interaction is strongest for S3 and weakest for S1 [40].

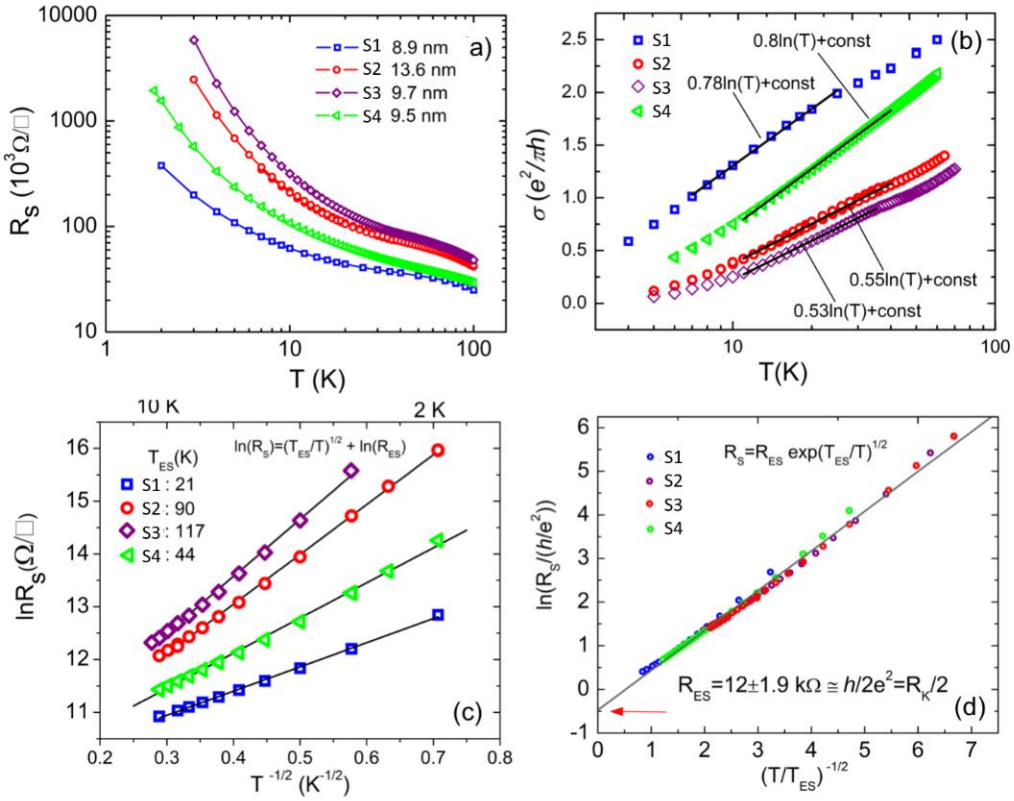

Figure 37: Electronic properties for S1 - S4

Below 10 K, R_S increases abruptly and can be described by Variable Range Hopping (Figure 37c). The data are well linearized in the coordinates lnR_s and $T^{-1/2}$ with two fitting parameters: T_{ES} (values shown on Figure 37c) and $R_{ES} \sim \frac{h}{2e^2} \equiv R_K/2$ (roughly sample-independent). T_{ES} reflects the effective strength of Coulomb interactions such that the stronger the EEI, the higher the crossover temperature to the Mott insulating behavior [23]. Even more, when $ln(R_S/R_K)$ is plotted against the dimensionless parameter $(T_{ES}/T)^{1/2}$, all traces of Figure 37c collapse onto a single line with an intercept of 1/2 as shown in Figure 37d. Thus, the insulating behavior is due to the Coulomb gap (depletion of states) induced in the single-particle density of states at the Fermi level by Coulomb interactions.

It appears that commensurate strain and low carrier concentrations strengthen EEI driving the system to an insulating state "earlier" (higher temperatures). For large distortions of the $SrTiO_3$ crystal structure and in-plane compressive strain, a Mott insulating phase is predicted but requires much higher doping level, 0.5 electrons/Ti atom [24] rather than the calculated ~0.01 electrons/Ti for our films. Although, screening is much less effective in 2d, EEI at such low electron concentrations would require that the Coulomb potential is sufficiently long-range for exchange interactions to be strong. Models that include full-range Coulomb forces predict that t_{2g} electrons at low concentrations in $SrTiO_3$-based interfaces or QW follow spontaneous orbital and spin order exhibiting correlated behavior [25, 26].

REFERENCES

1. Ohtomo, A. and H.Y. Hwang, *A high-mobility electron gas at the LaAlO3/SrTiO3 heterointerface.* Nature, 2004. **427**(6973): p. 423-426.

2. Herranz, G., et al., *High mobility in LaAlO3/SrTiO3 heterostructures: Origin, dimensionality, and perspectives.* Physical Review Letters, 2007. **98**(21).

3. Santander-Syro, A.F., et al., *Two-dimensional electron gas with universal subbands at the surface of SrTiO3.* Nature, 2011. **469**(7329): p. 189-193.

4. Kozuka, Y., et al., *Enhancing the electron mobility via delta-doping in SrTiO3.* Applied Physics Letters, 2010. **97**(22).

5. Cen, C., et al., *Nanoscale control of an interfacial metal-insulator transition at room temperature.* Nature Materials, 2008. **7**(4): p. 298-302.

6. Stemmer, S. and A.J. Millis, *Quantum confinement in oxide quantum wells.* Mrs Bulletin, 2013. **38**(12): p. 1032-1039.

7. Caviglia, A.D., et al., *Tunable Rashba Spin-Orbit Interaction at Oxide Interfaces.* Physical Review Letters, 2010. **104**(12).

8. McKee, R.A., F.J. Walker, and M.F. Chisholm, *Crystalline oxides on silicon: The first five monolayers.* Physical Review Letters, 1998. **81**(14): p. 3014-3017.

9. Laughlin, R.P., et al., *Magnetic and structural properties of BiFeO3 thin films grown epitaxially on SrTiO3/Si substrates.* Journal of Applied Physics, 2013. **113**(17).

10. Ohtomo, A., et al., *Artificial charge-modulation in atomic-scale perovskite titanate superlattices.* Nature, 2002. **419**(6905): p. 378-380.

11. Haeni, J.H., et al., *Room-temperature ferroelectricity in strained SrTiO3.* Nature, 2004. **430**(7001): p. 758-761.

12. Warusawithana, M.P., et al., *A Ferroelectric Oxide Made Directly on Silicon.* Science, 2009. **324**(5925): p. 367-370.

13. Chakhalian, J., et al., *Colloquium: Emergent properties in plane view: Strong correlations at oxide interfaces.* Reviews of Modern Physics, 2014. **86**(4): p. 1189-1202.

14. Moetakef, P., et al., *Toward an artificial Mott insulator: Correlations in confined high-density electron liquids in SrTiO3.* Physical Review B, 2012. **86**(20).

15. Baek, S.H. and C.B. Eom, *Epitaxial integration of perovskite-based multifunctional oxides on silicon.* Acta Materialia, 2013. **61**(8): p. 2734-2750.

16. Aguirre-Tostado, F.S., et al., *Elastic anomaly for SrTiO3 thin films grown on Si(001).* Physical Review B, 2004. **70**(20).

17. Cottier, R.J., et al., *Band gap tuning of epitaxial SrTiO3-delta/Si(001) thin films through strain engineering.* Applied Physics Letters, 2015. **107**(22).

18. Woicik, J.C., et al., *Ferroelectric distortion in SrTiO3 thin films on Si(001) by x-ray absorption fine structure spectroscopy: Experiment and first-principles calculations.* Physical Review B, 2007. **75**(14).

19. Li, H., et al., *Two-dimensional growth of high-quality strontium titanate thin films on Si.* Journal of Applied Physics, 2003. **93**(8): p. 4521-4525.

20. Tokura, Y., et al., *FILLING DEPENDENCE OF ELECTRONIC-PROPERTIES ON THE VERGE OF METAL MOTT-INSULATOR TRANSITIONS IN SR1-XLAXTIO3.* Physical Review Letters, 1993. **70**(14): p. 2126-2129.

21. Imada, M., A. Fujimori, and Y. Tokura, *Metal-insulator transitions.* Reviews of Modern Physics, 1998. **70**(4): p. 1039-1263.

22. Cottier, R.J., et al., *Phase coherence and electron-electron interactions in epitaxial, strained SrTiO3 films on Si(001).* Physical Review B (under revision), 2018.

23. Limouny, L., et al., *ANOMALOUS CROSSOVER FROM EFROS-SHKLOVSKII TO MOTT VARIABLE RANGE HOPPING IN SILICON MOSFETs.* Modern Physics Letters B, 2013. **27**(21).

24. Bjaalie, L., et al., *Turning SrTiO3 into a Mott insulator.* Physical Review B, 2014. **90**(19).

25. Tolsma, J.R., et al., *Quasiparticle mass enhancement and Fermi surface shape modification in oxide two-dimensional electron gases.* Physical Review B, 2016. **93**(4).

26. Tolsma, J.R., M. Polini, and A.H. MacDonald, *Orbital and spin order in oxide two-dimensional electron gases.* Physical Review B, 2017. **95**(20).

27. Zaumseil, P., *High-resolution characterization of the forbidden Si 200 and Si 222 reflections.* Journal of Applied Crystallography, 2015. **48**(2): p. 528-532.

28. Singh, S.D., et al., *Structural investigations of pulsed laser-deposited NiO epitaxial layers under different fluence values.* Journal of Materials Science, 2019. **54**(3): p. 1992-2000.

29. Corporation, R., *Integrated Thin Film Analysis Software GlobalFit 2.0: Extended Rocking Curve Analysis User Manual*. 2012.

30. Bowen D. K., T.B.K., *X-Ray Metrology in Semiconductor Manufacturing*. 2006: CRC Press Taylor & Francis Group.

31. Pohl, U.W., *Epitaxy of semiconductors : introduction to physical principles.* 2013.

32. Cullity, B.D., *Elements of X-ray Diffraction*. Second Edition ed. 1978: Addison-Wesley Publishing Company Inc.

33. Singh, S.D., et al., *Studies on structural and optical properties of pulsed laser deposited NiO thin films under varying deposition parameters.* Materials Science in Semiconductor Processing, 2017. **66**: p. 186-190.

34. Aruta, C., et al., *Interface reconstruction in superconducting CaCuO2/SrTiO3 superlattices: A hard x-ray photoelectron spectroscopy study.* Physical Review B, 2013. **87**(15): p. 8.

35. Ohnishi, T., et al., *Improved stoichiometry and misfit control in perovskite thin film formation at a critical fluence by pulsed laser deposition.* Applied Physics Letters, 2005. **87**(24).

36. Ohnishi, T., et al., *Defects and transport in complex oxide thin films.* Journal of Applied Physics, 2008. **103**(10).

37. Kim, Y.S., et al., *Sr flux stability against oxidation in oxide-molecular-beam-epitaxy environment: Flux, geometry, and pressure dependence.* Journal of Vacuum Science & Technology A, 2010. **28**(2): p. 271-276.

38. Hellman, E.S. and E.H. Hartford, *EFFECTS OF OXYGEN ON THE SUBLIMATION OF ALKALINE-EARTHS FROM EFFUSION CELLS.* Journal of Vacuum Science & Technology B, 1994. **12**(2): p. 1178-1180.

39. Choi, M., et al., *Strain relaxation in single crystal SrTiO3 grown on Si (001) by molecular beam epitaxy.* Journal of Applied Physics, 2012. **111**(6).

40. Zala, G., B.N. Narozhny, and I.L. Aleiner, *Interaction corrections at intermediate temperatures: Longitudinal conductivity and kinetic equation.* Physical Review B, 2001. **64**(21).